Dry-whip phenomenon in on-board rotordynamics: Modeling and experimentation

Yvon Briend, Eric Chatelet, Régis Dufour, Marie-Ange Andrianoely, Franck Legrand, Marcelo Samora Sousa, Valder Steffen, Sophie Baudin

To cite this version:

Yvon Briend, Eric Chatelet, Régis Dufour, Marie-Ange Andrianoely, Franck Legrand, et al.. Dry-whip phenomenon in on-board rotordynamics: Modeling and experimentation. Journal of Sound and Vibration, 2021, 513, 10.1016/j.jsv.2021.116398 . hal-03659963

HAL Id: hal-03659963
https://hal.science/hal-03659963v1

Submitted on 16 Oct 2023

Version of Record: https://www.sciencedirect.com/science/article/pii/S0022460X21004478
Manuscript_0cfacb2393a224ce9c1395a29e56508e

Dry-whip phenomenon in on-board rotordynamics: modelling and experimentation

Yvon Briend[1,*], Eric Chatelet[1], Régis Dufour[1], Marie-Ange Andrianoely[1], Franck Legrand[1], Marcelo Samora Sousa Jr[2], Valder Steffen Jr[2], Sophie Baudin[3]

Abstract

This paper addresses rotor-stator contact issues, especially the dry-whip phenomenon, as caused by base excitations. So far, this particular instability in the case of direct rub between shaft and stator was only shown by experiments to occur in response to mass unbalance excitation during run-up or run-down and/or to external disturbance such as direct impact applied to the rotor. The present paper aims to demonstrate that it can also be triggered by external forces coming from the rigid base motion. To this end, both numerical and experimental approaches are employed. A rotor finite element model combining on-board motions with shaft-stator rub impact is first proposed. This model is validated with a rotor test-rig supported by hydrodynamic bearings and mounted on a multi-axial hydraulic shaker and subject to a harmonic base motion. The dry-whip is then shown experimentally by using a base shock excitation consisting of two transverse translations, which is later confirmed numerically. The influence of important parameters on the dynamic behavior of the system is also assessed, such as the hydrodynamic bearing nonlinearities, the amplitude and direction of the base translations and the dry friction coefficient.

Keywords: On-board rotor, Rotor-stator rubbing, Dry-whip, Experimental validation, Hydrodynamic bearing, Multi-axial excitations

---

1. INTRODUCTION

Rotating machinery plays a major role in plenty of industrial fields, such as automotive, defense, energy, space, etc. In such fields, the need for designing rotating systems always lighter and more robust is constantly increasing since it inherently permits reducing the need for power consumption. However, this often leads to more compact structures having smaller rotor-stator clearances. Consequently, this increases the possibility of rotor-stator contact phenomena, such as those that may occur between a centrifugal compressor impeller and casing, labyrinth seals and sealing housing, turbine blades and casing, etc. These contact phenomena may be responsible for diverse harmful nonlinear behaviors such as sudden jumps, modal interactions, super-harmonics, isola, chaotic motions, which can threaten the structural integrity. A particular example includes the well-known dry-whip phenomenon, characterized by a rolling-sliding state in backward whirl of the rotor onto the stator that results in critical amplitudes and high frequencies of vibration. This instability can be triggered by many sources of excitations, e.g. a sudden mass unbalance due to blade loss, direct impacts on the shaft, rotor drops due to active magnetic bearings (AMBs) failures and base motions.

The study of rotor-stator contact and its underlying nonlinear phenomena is not recent and has constantly raised a lot of attention. A first notable progress may be attributed to the work done by Black [1] who used

---

[*] Corresponding author: yvon.briend@insa-lyon.fr
[1] Univ Lyon, INSA Lyon, CNRS, LaMCoS, UMR5259, 69621 Villeurbanne, France
[2] LMEst-Structural Mechanics Laboratory, School of Mechanical Engineering, Federal University of Uberlândia, Av. João Naves de Ávila, 2121, Uberlândia, MG 38408-196, Brazil
[3] AVNIR Engineering, 62 Boulevard Niels Bohr, 69603 Villeurbanne Cedex, France

Preprint submitted to Journal of Sound and Vibration *July 27, 2021*

an analytical approach to determine the domains of existence of the dry-whirl and dry-whip in terms of the friction coefficient with respect to the rotor speed of rotation. Lingener [2] investigated experimentally several configurations of a rotor with a shiftable mass and a stator with adjustable stiffness. He showed that the backward whirl can be triggered either with only mass unbalance or with an external hit. Later, Bently *et al.* [3, 4] also proved that dry-whip can be initiated by hammer impacts at very low speeds or without external disturbance for low rotor-stator clearance. The same year, Choi [5] highlighted the same phenomena for two types of stator in aluminium and acrylic. Besides, the author confirmed the major influence of the friction coefficient and the mass unbalance value on the appearance of the dry-whip. Childs and Bhattacharya [6] and later Wilkes *et al.* [7] extended the model of Black [1] to multi-mode rotors. They also investigated both experimentally and numerically the transition between dry-whirl and dry-whip and why these transitions may not be the same when comparing a run-up and a run-down. In the same decade, Jiang [8] provided, with a Jeffcott rotor model, the domains of existence and co-existence of the different rotor-stator contact phenomena with respect to the friction coefficient and to the stator stiffness. In particular, the regions where the dry-whip can be triggered by either mass unbalance or external disturbance were clearly identified. For further complete overview about contact rotordynamics, extensive and recent reviews may be found in [9–11].

In the last few years, research efforts dedicated to the dry-whip phenomenon have intensified even more. For instance, Hong *et al.* [12] and then Yu *et al.* [13] used the complex nonlinear modes approach of Laxalde and Thouverez [14] to explain the dry-whip as the instability of one backward whirl mode, i.e. when its modal damping becomes negative with the increase of the modal shape amplitude. They succeeded to apply their method to a 8-node finite element model (FEM) of a Bently-rotor test rig. Wang *et al.* [15] proposed a new approach based on Filippov's convex method to distinguish the rolling and sliding states in a typical dry-whip period. They concluded that it was quite difficult to detect experimentally a pure rolling state as that presented in [3]. Bezhad and Alvandi [16] proposed a non-circular clearance solution with a three-lobed shape to modify the dry-whip characteristics such as its amplitude and frequency. They successfully demonstrated both experimentally and numerically the efficiency of their solution, reaching a reduction of the dry-whip amplitude of more than 50 % or having the dry-whip that quickly disappeared by itself with time. Lastly, Ehehalt *et al.* [17] evidenced experimentally with a very modular test rig the coexistence of several dry-whip modes with different characteristics. All other typical nonlinear phenomena such as jumps, super or sub-harmonics and full annular synchronous whirl were observed.

Studies about the influence of base motion on rotordynamics started in the 80s [18, 19] from a global concern regarding seismic excitation from earthquake occurring in the vicinity of power plants. This type of excitation is another source of rotor-stator contacts; however, literature on these combined effects is less abundant. Among the few contributions, Hou *et al.* [20] simulated the dynamics of an aircraft rotor mounted on nonlinear supports and subject to rub-impacts. They showed with their 4-DOF model that the combination of the contacts and an airflight maneuver, represented by a yaw rotation with constant angular speed, is able to trigger a sub-harmonic resonance of the system. In a similar context, Gao *et al.* [21] recently reproduced experimentally barrel roll airflight maneuvers on their on-board rotor test rig equipped with a rub-impact ring mounted around the disk. By means of specific dynamics tools such as wavelet scalograms and spectrum cascades, they evidenced that the roll base excitation tends to increase the rotor lateral responses and the number of sub-harmonics of the shaft speed of rotation. Moreover, the amplitude of these sub-harmonics was shown to vary with time according to the existence of contacts which were directly influenced by the variation of the gravity direction. Lastly, Jarroux *et al.* [22] validated experimentally their model of a rotor mounted on AMBs protected by touch down bearings (TDBs) in case of levitation failure or strong base motions. Good agreements were observed with a 1.1 g harmonic vertical base translational acceleration for several shaft speeds of rotation and with shock vertical excitation of 3.1 g, even when the shaft impacted the inner ring of the TDBs. Su *et al.* [23] investigated numerically the same type of rotor supported by AMBs and TDBs. They showed from diverse cases of translational shock base motions that transitions between different regimes of rebounds, backward whirl and dry-whip were likely to occur.

So far, as it was previously pointed out, contributions devoted to the experimental validation of on-board rotor models including shaft-stator rub are rare in the literature. Regarding the harmful nonlinear dry-whip phenomenon, it was only evidenced experimentally when triggered by mass unbalance during a run-up or run-down of the shaft speed of rotation [5–7], and/or by an external disturbance such as a hammer impact [2–4, 7, 13, 16, 17] or a solenoid actuator [24]. In this context, the present article proposes first a FEM of an on-board rotor able to simulate the shaft-stator rub due to a rigid base excitation. This model consists of a rotor-hydrodynamic bearing system involving an original contact law for modelling the possible shaft-stator rub. A first experimental validation is performed with a harmonic base translation resulting in one unilateral contact. Then the possibility to trigger a dry-whip instability is shown both experimentally and numerically by combining mass unbalance and mono- or multi-axial shock base motions, with a stationary shaft speed of rotation. Furthermore, the influence of important parameters on the system's dynamics, such as the hydrodynamic bearing nonlinearities, the dry friction coefficient, the base motion direction and amplitude, is assessed.

2. MODELLING

In order to represent the on-board rotor dynamics, two reference frames must be used as illustrated in Fig. 1. The first one, $\mathcal{R}_0(O_0, \vec{X}_0, \vec{Y}_0, \vec{Z}_0)$, is considered as Galilean. The second one, $\mathcal{R}(O, \vec{x}, \vec{y}, \vec{z})$, is fixed to the rotor base and independent of the shaft's rotation. Its origin O is located at the left end of the shaft neutral axis and $\vec{y}$ coincides with the shaft axis of rotation at rest. One-dimensional Timoshenko beam elements are used to model the shaft. Each element possesses two nodes and six DOFs per node which are (u, w) the bending transverse displacements along $(\vec{x}, \vec{z})$ respectively, v the axial displacement in $\vec{y}$, (ψ, θ) the bending transverse rotations around $(\vec{z}, \vec{x})$ respectively and β the torsion angle of rotation around $\vec{y}$. All these displacements depend only on the axial coordinate y and the total shaft speed of rotation $\dot{\phi}$ is defined as $\dot{\phi}(y) = \dot{\phi}^* + \dot{\beta}(y)$ where $\dot{\phi}^*$ is the constant nominal shaft speed of rotation provided by the motor. Cubic and quadratic shape functions are employed to approximate (u, w) and (ψ, θ), respectively, while linear shape functions are used for v and β. Applying the Lagrange's equations to all the energies and virtual works of the system leads to the derivation of the following system of equations governing the rotor dynamics:

$$\mathbf{M}\ddot{\boldsymbol{\delta}} + \Big(\mathbf{G} + \mathbf{C} + \mathbf{C_{ba}}\Big)\dot{\boldsymbol{\delta}} + \Big(\mathbf{K} + \mathbf{K_{ba}}\Big)\boldsymbol{\delta} = \mathbf{F_g} + \mathbf{F_u} + \mathbf{F_{ba}} + \mathbf{F_{jb}} + \mathbf{F_c} \tag{1}$$

with $\mathbf{M}$, $\mathbf{G}$, $\mathbf{C}$ and $\mathbf{K}$ the classical mass, gyroscopic, structural damping and structural stiffness matrices respectively, $\mathbf{F_u}$ the classical mass unbalance force vector and $\boldsymbol{\delta}$ the global DOF vector. The structural damping matrix $\mathbf{C}$ is taken proportional to $\mathbf{K} = \mathbf{K_b} + \mathbf{K_v} + \mathbf{K}_\beta$ so that $\mathbf{C} = c_b\mathbf{K_b} + c_v\mathbf{K_v} + c_\beta\mathbf{K}_\beta$ where $\mathbf{K_b}$, $\mathbf{K_v}$ and $\mathbf{K}_\beta$ are the structural stiffness matrices related to bending, axial and torsional effects, respectively and c_b, c_v and c_β are coefficients to adjust. $\mathbf{C_{ba}}$, $\mathbf{K_{ba}}$ and $\mathbf{F_{ba}}$ are respectively the time-dependent damping and stiffness matrices and the force vector related to the base motion [25]. $\mathbf{F_g}$ is a force vector related to the gravity load, which may depend on time in the case of a rotational base motion. $\mathbf{F_{jb}}$ is the load vector which contains the nonlinear restoring forces provided by the journal bearings. Although in this study the bearings have a finite length, their corresponding forces are computed by using the short-bearing hypothesis [26] in order to reduce the time costs of the further analysis. Gümbel's boundary conditions are employed, taking into account the variation of the positive pressure interval due to the dynamic eccentricities and attitude angles as found in [27]. In the sequel, it is assumed that the journal bearing centers are on the axis $(O\vec{y})$.

$\mathbf{F_c}$ is the load vector that contains the nonlinear forces from the likely rotor-stator contacts with circular rings fixed to the rotor base. In this paper, these forces are based on the developments depicted in [28, 29] which use a penalty law. To understand the contact phenomenon, a sketch of the shaft rotating inside a circular ring of axial coordinate y_B in $\mathcal{R}$ is shown in Fig. 2a. The shaft is in quasi-static equilibrium (shaft rotating at fixed speed but without external dynamic excitation) at the location S of coordinates (u_S, y_B, w_S) in $\mathcal{R}$. Due

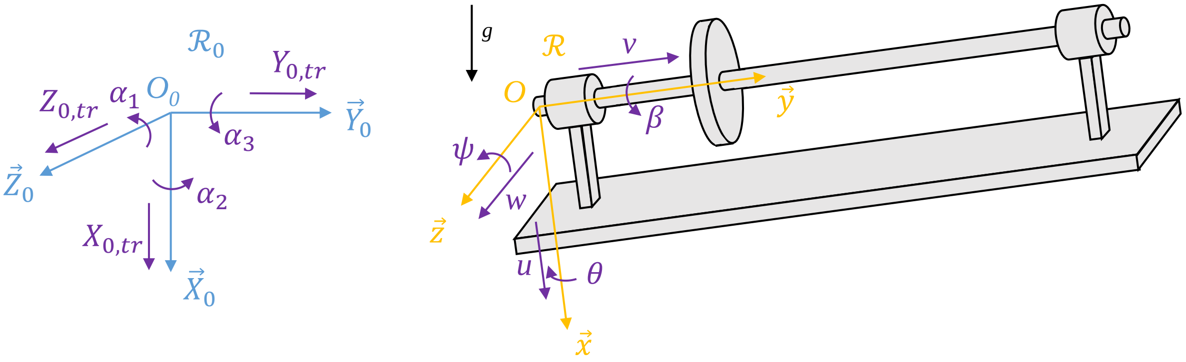

Figure 1. Sketch of an on-board rotor mounted on a rigid and moving base

to external excitations such as mass unbalances and base motions, the shaft center A of coordinates (u, y_B, w) in $\mathcal{R}$ orbits around S with an eccentricity $e_S = (u_{SA}^2 + w_{SA}^2)^{1/2}$ with $u_{SA} = u - u_S$ and $w_{SA} = w - w_S$. Unlike in [28, 29], S may not necessarily coincide with the ring center B. In this context, the location of B can be given either with respect to S with $\overrightarrow{SB} = x_{SB}\vec{x} + z_{SB}\vec{z}$ or with respect to O with $\overrightarrow{OB} = x_{OB}\vec{x} + z_{OB}\vec{z}$. These two definitions of B will be used in Section 3.1 to define the different contact rings. Then, contact occurs when the shaft eccentricity $e_B = (u_{BA}^2 + w_{BA}^2)^{1/2}$ is greater than the radial clearance $c_b = R_c - R_s$, where $u_{BA} = u_{SA} - x_{SB} = u - x_{OB}$ and $w_{BA} = w_{SA} - z_{SB} = w - z_{OB}$. Furthermore, in contrast with [28, 29], the normal component $f_{cn} = f_{cnk} + f_{cnc}$ of each contact force is herein computed from nonlinear contact stiffness and damping with a half-sine law instead of an arctangent law, according to :

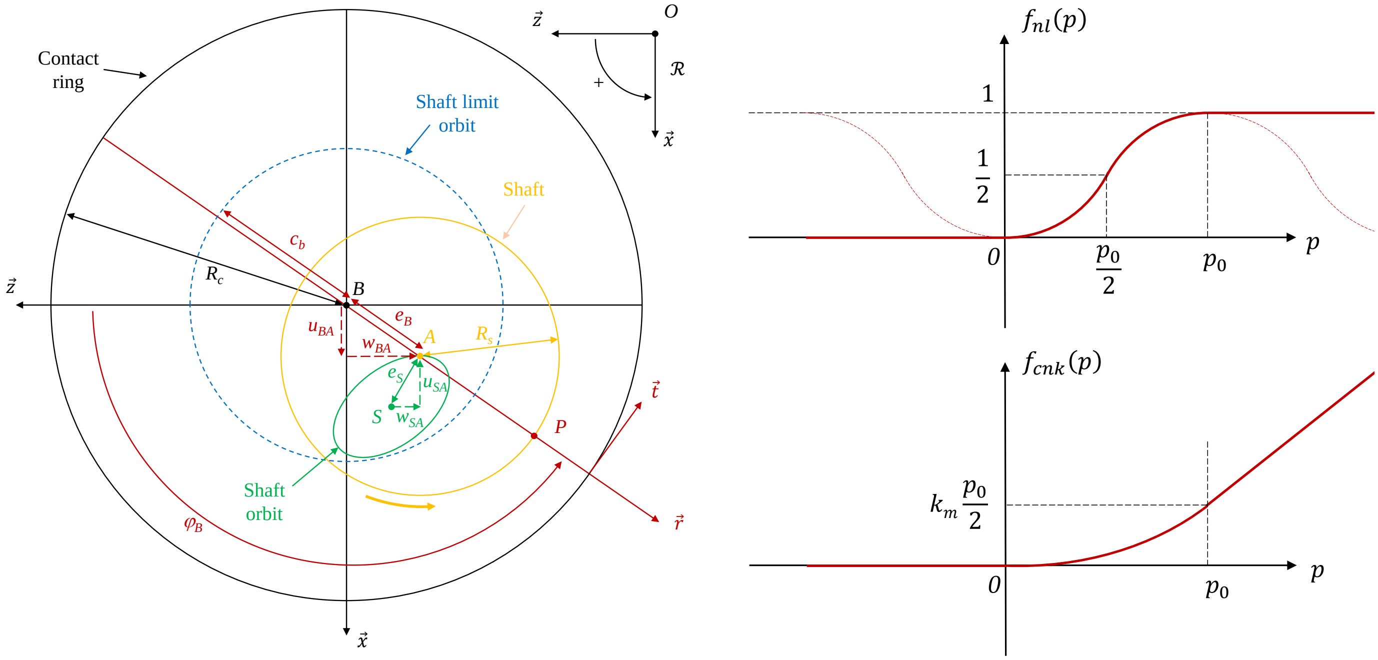

(a) (b)

Figure 2. (a) Sketch of the shaft rotating inside a circular contact ring and (b) Nonlinear half-sine function $f_{nl}(p)$ and normal contact stiffness force f_{cnk}

$$f_{cnk}(p) = k_m \int_0^p f_{nl}(p)\mathrm{d}p \quad ; \quad f_{cnc}(p, \dot{p}) = c_m f_{nl}(p)\dot{p} \tag{2}$$

with $p = e_B - c_b$ representing the contact penetration, k_m and c_m the maximum value of stiffness and damping, respectively, and

$$f_{nl}(p) = \begin{cases} 0 & \forall p < 0 \\ \frac{1}{2}\left[1 + \cos\left(\pi\left(\frac{p}{p_0} + 1\right)\right)\right] & \forall p \in [0; p_0[\\ 1 & \forall p \geq p_0 \end{cases} \tag{3}$$

The parameter p_0 permits adjusting the slope of the nonlinear half-sine function $f_{nl}(p)$ so as to facilitate the convergence of the numerical algorithm (see Fig. 2b). This half-sine profile prevents from the appearance of negative normal contact force for $p < 0$.

The tangential contact force, axial contact force and contact moments are then computed from the normal contact force f_{cn} as in [29]. The global nonlinear equation of motion (1) is solved by using a classical Newmark integration in combination with a Newton-Raphson scheme. The time step for the integration is allowed to vary in order to handle the strong nonlinearities and the numerical results are then re-sampled with a fixed time step corresponding to the sampling frequency of the experimental measurements. Regarding the initial conditions, the system is supposed to be at the quasi-static equilibrium position with a constant shaft speed of rotation at $t = 0$ s. After $t \geq 0$ s, the mass unbalances are imposed suddenly. The base excitation are only imposed once the transient state due to the appearance of the mass unbalances has vanished.

3. EXPERIMENTAL AND NUMERICAL INVESTIGATIONS

3.1. Presentation of the rotor test-rig

The test rig used for the experimental validations and investigations is shown in Fig. 3. The rotor is composed of a steel-CF53 shaft, two disks, two hydrodynamic bearings, a DC-electric motor and a flexible coupling between the shaft and the motor. The whole system is mounted on a thick plate fixed to a 6-DOF hydraulic shaker able to reproduce different types of rotor base excitation. The data corresponding to these elements, used in the further numerical computations, is available in Table 1. The characteristics of the motor-shaft coupling, which come either from the manufacturer or from an optimization through a preliminary modal analysis, are shown in Table 2. Mass unbalances are added to the two disks according to the data shown in Table 3. In the absence of base motion, these mass unbalances are not sufficient to induce any contact. The shaft is discretized into 28 finite elements as shown by its mesh in Fig. 4 and the node coordinates are given in Table 4. While the main shaft diameter is 12.7 mm, the first three and last four finite elements possess a diameter of 12 mm. The hydrodynamic bearings have finite lengths with a length-to-diameter ratio of ≈ 0.70. No feeding pressure is taken into account since it is reasonably low (0.4 bar) and out of the scope of the analytical short bearing approximation.

Shaft length and diameters	851 mm; 12.7 mm or 12 mm
Shaft Young modulus and Poisson coefficient	210 GPa; 0.3
Shaft and disk density	7778 kg/m^3
Radius and thickness of disks	63.1 mm; 15.6 mm
Hydrodynamic bearing radius, length and radial clearance	6.39 mm; 9 mm; 40 µm
Hydrodynamic bearing oil viscosity	0.0206 Pa.s

Table 1. Main rotor data

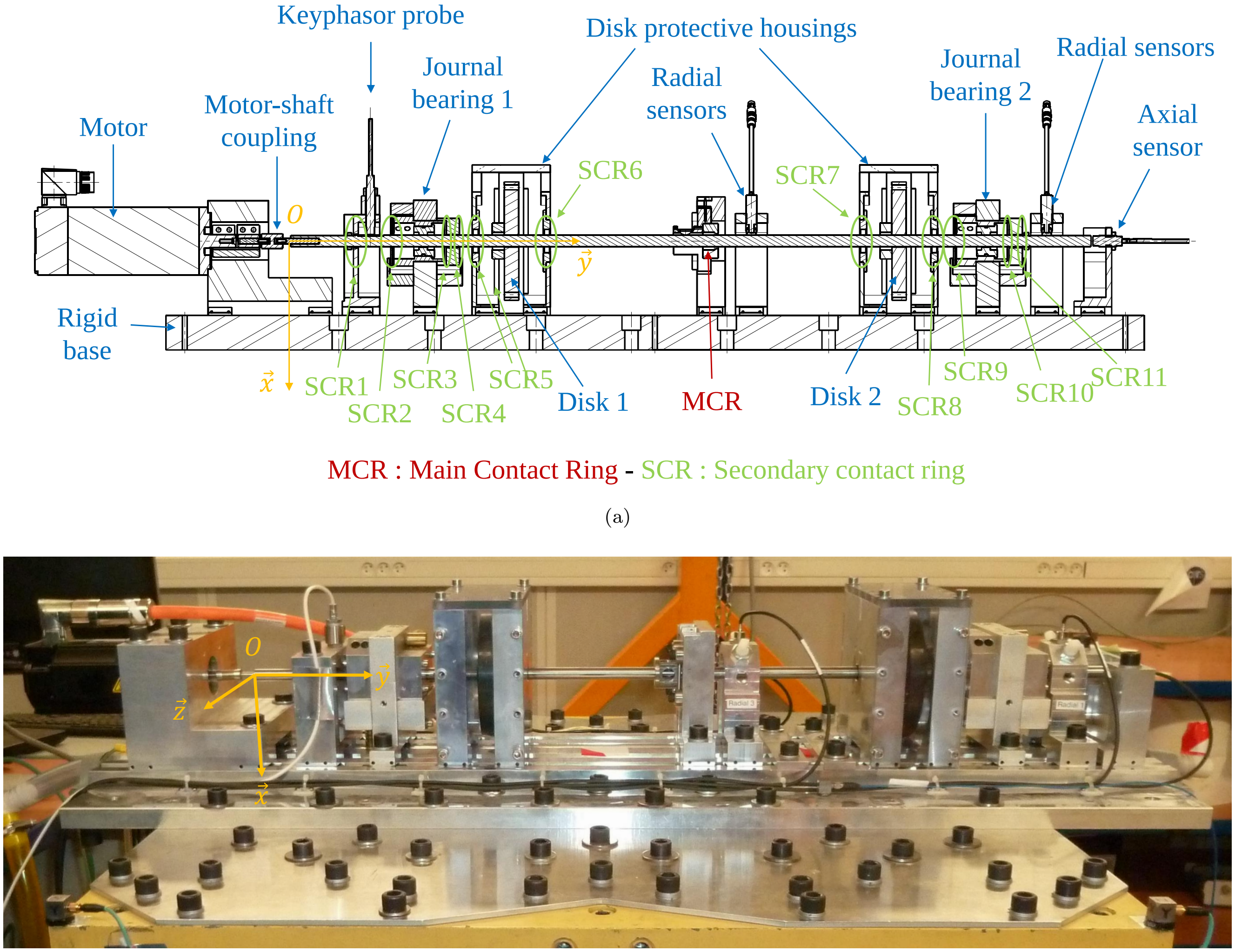

(a)

(b)

Figure 3. On-board rotor test bench used for the experimental validations: (a) CAD view and (b) Photo view

Stiffness	Value	Damping	Value
K_{uu}	1000 N/m	C_{uu}	0 N.s/m
K_{vv}	2500 N/m	C_{vv}	4 N.s/m
K_{ww}	1000 N/m	C_{ww}	0 N.s/m
$K_{\theta\theta}$	0.21 N.m/rad	$C_{\theta\theta}$	1x10^{-3} N.m.s/rad
$K_{\psi\psi}$	0.21 N.m/rad	$C_{\psi\psi}$	1x10^{-3} N.m.s/rad
$K_{\beta\beta}$	27 N.m/rad	$C_{\beta\beta}$	1x10^{-2} N.m.s/rad

Table 2. Motor-shaft coupling characteristics of the rotor test bench

Mass unbalance	On node	Radius	Phase
2.37 g	10	57 mm	0 °
2.37 g	10	57 mm	-20 °
2.37 g	20	57 mm	0 °
2.37 g	20	57 mm	-20 °

Table 3. Mass unbalance configuration

In order to obtain rotor-stator contact, the test bench was equipped at the middle of the shaft with a circular ring (see MCR for Main Contact Ring in Fig. 3a) made of prehardened steel (W-Nr.1.2099 or EN-X7Cr13+S+QT). As illustrated in Fig. 5, the contact area of this ring is a torus having a semi-circular section in order to generate a punctual contact with the shaft in case of too high radial vibration level. The ring is

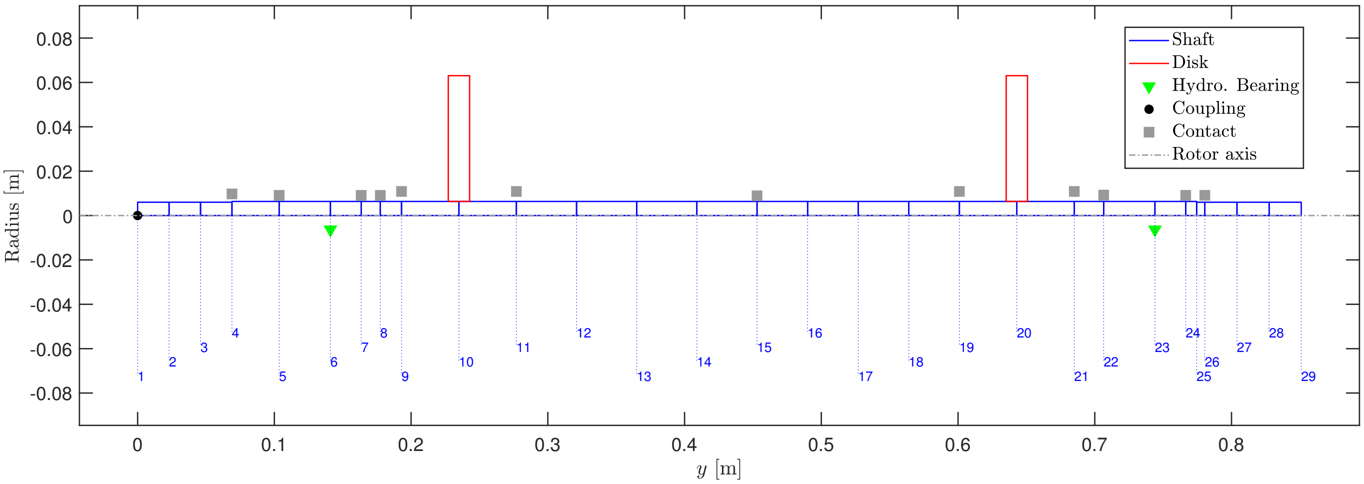

Figure 4. FE mesh of the on-board rotor with contact rings

Nodes 1 to 10 [mm]	0	23	46	69	103.5	141	163.5	177.5	193	235
Nodes 11 to 20 [mm]	277	321	365	409	453	490	527	564	601	643
Nodes 21 to 29 [mm]	685	706.5	744	766.5	744.5	780.5	804	827.5	851	-

Table 4. Axial coordinates in $\mathcal{R}$ of the finite element nodes

mounted with a tight fit into a housing itself integrated into a support fixed to the rotor rigid base. By moving five refined screws, the MCR fixed to the housing can be centered almost perfectly with respect to the quasi-static equilibrium position of the shaft, i.e., superimposing B and S of Fig. 2a. The remaining small gap between B and S can be measured precisely and introduced then in the model in terms of the coordinates (x_{SB}, z_{SB}). All the data corresponding to the MCR is available in Table 5. As it will be seen in the following analysis in the case of dry-whip, contact may also occur at other locations owing to larger transverse displacements of the shaft. This new contact points, named as Secondary Contact Ring (SCR), are shown in Fig. 3a and recalled in Fig. 4. They correspond to the circular bores of some supports or of protective housings (disks or hydrodynamic bearing) all made in steel. As they were not initially intended for rotor-stator contact, the coordinates of their center B could not be measured in contrast to the MCR. Regarding the dry friction coefficient μ, no distinction is made between static and dynamic coefficients. For the SCRs, those closest to the hydrodynamic bearings have a small value $\mu = 0.05$ as due to oil projection on the shaft, while others near the disk have a more standard value of steel-steel dry contact with $\mu = 0.25$. With regards to the MCR, the friction coefficient is not given here since it is adjusted depending on the test.

The test bench is instrumented with several sets of sensors. First, four inductive sensors are distributed by pair in two supports to measure on a plane the radial bending displacements of the shaft. The two sensors of each support are directed along $\vec{x}$ and $\vec{z}$ of $\mathcal{R}$ to retrieve the shaft orbits. One support is located at Node 16 so as to be the closest to the MCR and the other is placed at Node 27 where the shaft's response is expected to be important (free boundary condition). Secondly, another inductive sensor near Node 4 is employed as a keyphasor probe for detecting an axial groove on the shaft. This sensor is directed along $\vec{x}$. This means that the keyphasor pulses occur when the axial groove crosses the axis $-\vec{x}$, which is considered then as the 0 ° reference shaft angular position with $\phi^* = 0$ °. Thirdly, a last inductive sensor is used to measure the axial rigid-body displacement of the shaft. It is located at Node 29 and directed along $-\vec{y}$. Finally, four tri-axial accelerometers located at the four corners of the upper face of the 6-DOF shaker are used both for the excitation driving process and to determine the shaker's real motion, which is afterwards introduced into the FEM. All the signals

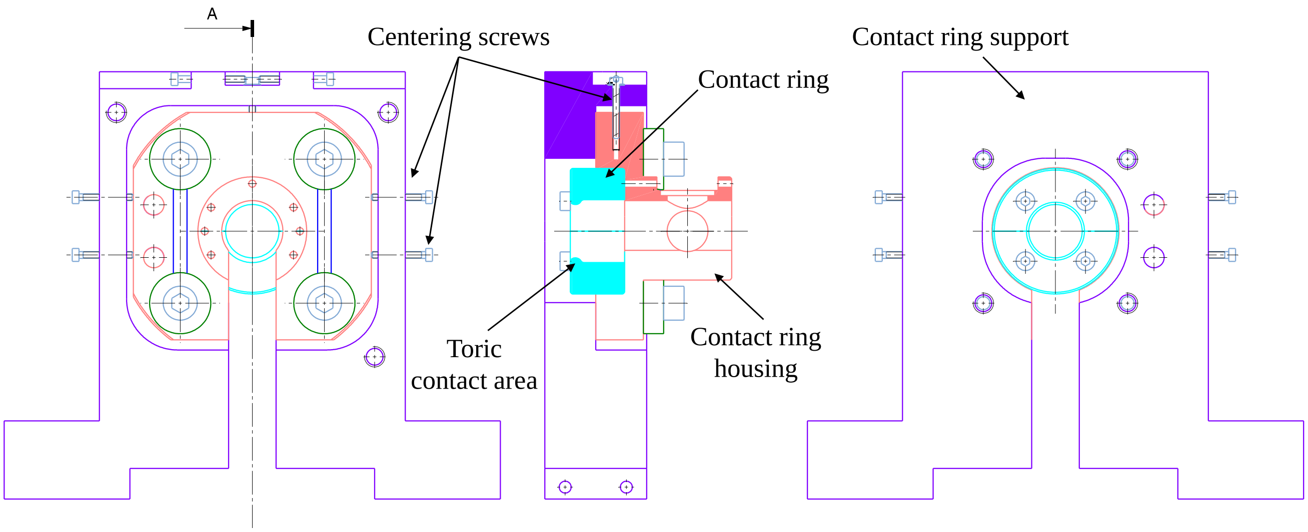

Figure 5. Focus on the MCR assembling

Contact ID	Clearance c_b [μm]	Max. Stiff. k_m [N/m]	Max. Damp. c_m [N.s/m]	Slope param. p_0 [μm]	Friction coef. μ	Location of B [μm]
MCR (Node 15)	500	1×10^{10}	1×10^{4}	0.1	-	$x_{SB} = -13.6$ $z_{SB} = 3.2$
SCR1 (Node 4)	1150	1×10^{10}	1×10^{4}	0.1	0.05	$x_{OB} = 0$ $z_{OB} = 0$
SCR2 (Node 5)	650	1×10^{10}	1×10^{4}	0.1	0.05	$x_{OB} = 0$ $z_{OB} = 0$
SCR3 (Node 7)	650	1×10^{10}	1×10^{4}	0.1	0.05	$x_{OB} = 0$ $z_{OB} = 0$
SCR4 (Node 8)	650	1×10^{10}	1×10^{4}	0.1	0.05	$x_{OB} = 0$ $z_{OB} = 0$
SCR5 (Node 9)	2000	1×10^{10}	1×10^{4}	0.1	0.25	$x_{OB} = 0$ $z_{OB} = 0$
SCR6 (Node 11)	2000	1×10^{10}	1×10^{4}	0.1	0.25	$x_{OB} = 0$ $z_{OB} = 0$
SCR7 (Node 19)	2000	1×10^{10}	1×10^{4}	0.1	0.25	$x_{OB} = 0$ $z_{OB} = 0$
SCR8 (Node 21)	2000	1×10^{10}	1×10^{4}	0.1	0.25	$x_{OB} = 0$ $z_{OB} = 0$
SCR9 (Node 22)	650/750	1×10^{10}	1×10^{4}	0.1	0.05	$x_{OB} = 0$ $z_{OB} = -150$
SCR10 (Node 24)	650	1×10^{10}	1×10^{4}	0.1	0.05	$x_{OB} = 0$ $z_{OB} = 0$
SCR11 (Node 26)	1000	1×10^{10}	1×10^{4}	0.1	0.05	$x_{OB} = 0$ $z_{OB} = 0$

Table 5. Contact ring parameters - specified, measured or adjusted

from these sensors are sampled at 4096 Hz on the same data acquisition system.

In the following tests, the shaft speed of rotation is constant with $\dot{\phi}^* = 1700$ rpm and the shaft rotates in the direct sense, i.e. from $\vec{z}$ to $\vec{x}$. The rotor thus runs in a sub-critical regime since the first critical speed is around 2400 rpm. The shaft speed frequency of rotation 1700/60 Hz is noted X. The phase angles of the mass unbalances in Table 3 are given with respect to the axial groove used for the keyphasor probe. The initial time $t = 0$ s always corresponds to a keyphasor pulse with $\phi^* = 0$ ° with a steady-state mass unbalance response. The phase of the base motions with respect to the mass unbalance is not known a priori since the shaker's motion was started at any arbitrary moment while the shaft was already rotating in steady state. However, it can be found afterwards by post-processing the measurements since the keyphasor probe and the accelerometers are sampled synchronously. The orientation of $\mathcal{R}_0$ and $\mathcal{R}$ is defined to be strictly the same, i.e, with $\vec{X}_0 = \vec{x}$, $\vec{Y}_0 = \vec{y}$ and $\vec{Z}_0 = \vec{z}$, when the shaker is at rest. Only base motion composed of translations are scheduled, however negligeable rotations may also exist. The coefficient for the structural damping were obtained through a preliminary modal analysis so that $c_b = c_v = c_\beta = 1 \times 10^{-5}$. All the orbits are presented by looking at them from the free shaft end toward the motor, as in Fig. 2a. Furthermore, the orbits of Node 16 are centered around the point B of the MCR, i.e., by assessing (u_{BA}, w_{BA}), while those of Node 27 are centered around the static equilibrium position S of this node, i.e., by assessing (u_{SA}, w_{SA}). Lastly, all the experimental results presented in the sequel are not filtered nor processed with windowing functions.

3.2. Unbalance response on fixed base

Before considering any base excitation, a response to the mass unbalances only is addressed. This study permits quantifying the gap between the shaft and the MCR without base motion, having a preliminary and necessary validation of the model, and highlighting the influence of the hydrodynamic bearing nonlinearities. To this end, the experimental and nonlinear numerical shaft orbits at Nodes 16 and 27 are shown in Fig. 6a and Fig. 6b, respectively. In addition, the limit orbit at Node 15 as illustrated in Fig. 2a is added to Fig. 6a and the predicted orbits when the restoring forces of the hydrodynamic bearings are linearized are added for both Nodes 16 and 27. Finally, the orbit at Node 25 is also presented in Fig. 6b in order to emphasize the nonlinearity of the orbit shapes. These orbits are all shown over a time period of 0.21 s, i.e. six shaft revolutions. The shaft position on its respective orbit when the keyphasor pulse is detected experimentally (or numerically with $\phi^* = 0$ °) is also displayed.

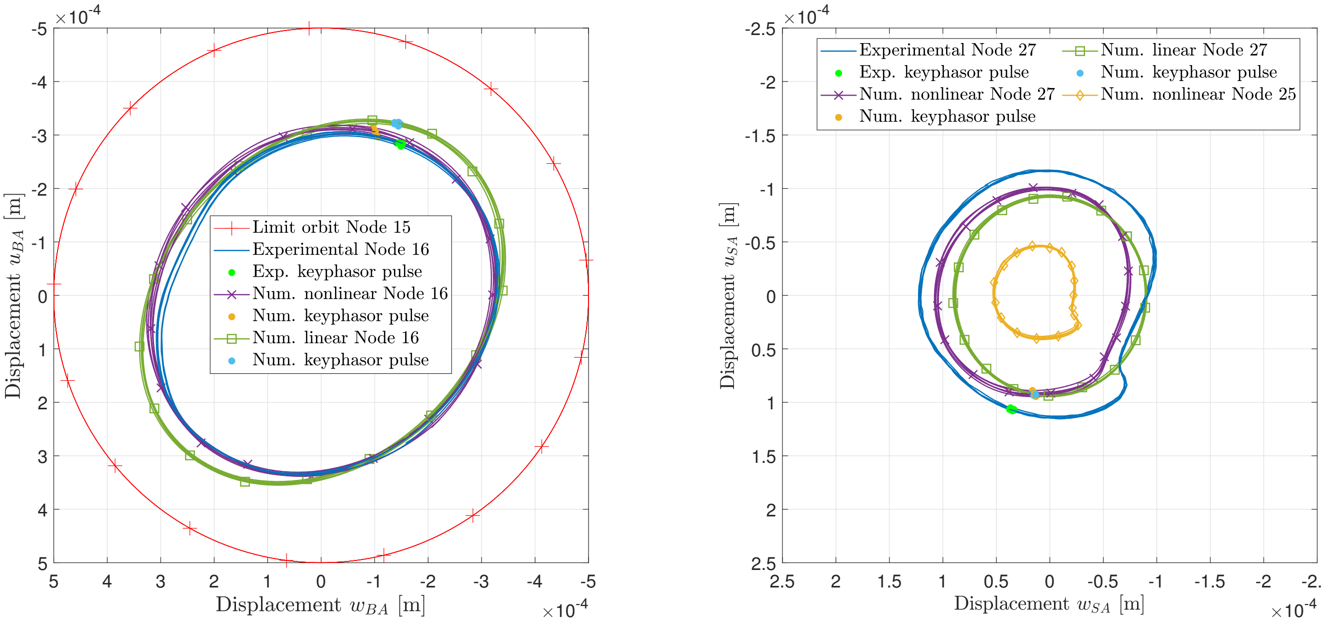

(a)

(b)

Figure 6. Predicted and measured shaft responses over 0.21s (6 shaft revolutions) to mass unbalance with $\dot{\phi}^* = 1700$ rpm: (a) Node 16 and (b) Node 27

Firstly, it is seen in Fig. 6a that the actual mass unbalance configuration is not high enough to induce any contact by itself. Contact can neither occur in the other SCRs since they are closer to the hydrodynamic bearings and because the shaft is mostly deforming on its first mode with a maximum transverse displacement near the MCR. Secondly, the nonlinearities in the journal bearings are shown to be quite influent on the predicted orbits since the corresponding orbits are no longer perfectly circular or elliptic as they are in the linear case. Moreover, the nonlinear orbits are much closer to the experimental orbits. This can be mostly highlighted in Fig. 6b for Node 27 whose nonlinear numerical orbit exhibits a similar deformed shape at the right bottom corner as in the experimental orbit. This specific measured shape is even more similar to that of Node 25, however with a lower amplitude since it is closer to the journal bearing. Therefore, it becomes clear that nonlinearities in the hydrodynamic bearings must be accounted for numerically in the further tests. Regarding the shaft position on its orbit at the keyphasor pulses, excellent experimental-numerical agreements are also noted. Furthermore, as expected, it is noteworthy that these shaft positions are located at the top at Node 16 while they are at the bottom at Node 27 since the shaft mostly deforms on its first bending mode and the second hydrodynamic bearing generates a phase shift between these two nodes. In fact, the shaft positions at Node 16 are located in the vicinity of an angle of -20 ° with respect to $-\vec{x}$ owing to the mass unbalance phases. Hence, it can be concluded that the nonlinear model is already well representative without base motion.

3.3. Harmonic base motion

The rotor is now subject to the mass unbalance and to a harmonic base motion composed of a transverse translation acting along $\vec{Z}_0$ according to $Z_{0,tr} = A_Z \cos(2\pi f_Z t + \varphi_Z)$ with $A_Z = 707$ µm and $f_Z = 0.5X \approx 14.17$ Hz. The phase φ_Z is found to be approximately -145 °. The value of μ for the MCR has not much influence on this analysis, it is then fixed to $\mu = 0.4$ as it will be used in the next section. The predicted and measured shaft orbits at Nodes 16 and 27 are plotted over a time period of 0.21 s in Fig. 7a and Fig. 7b, respectively.

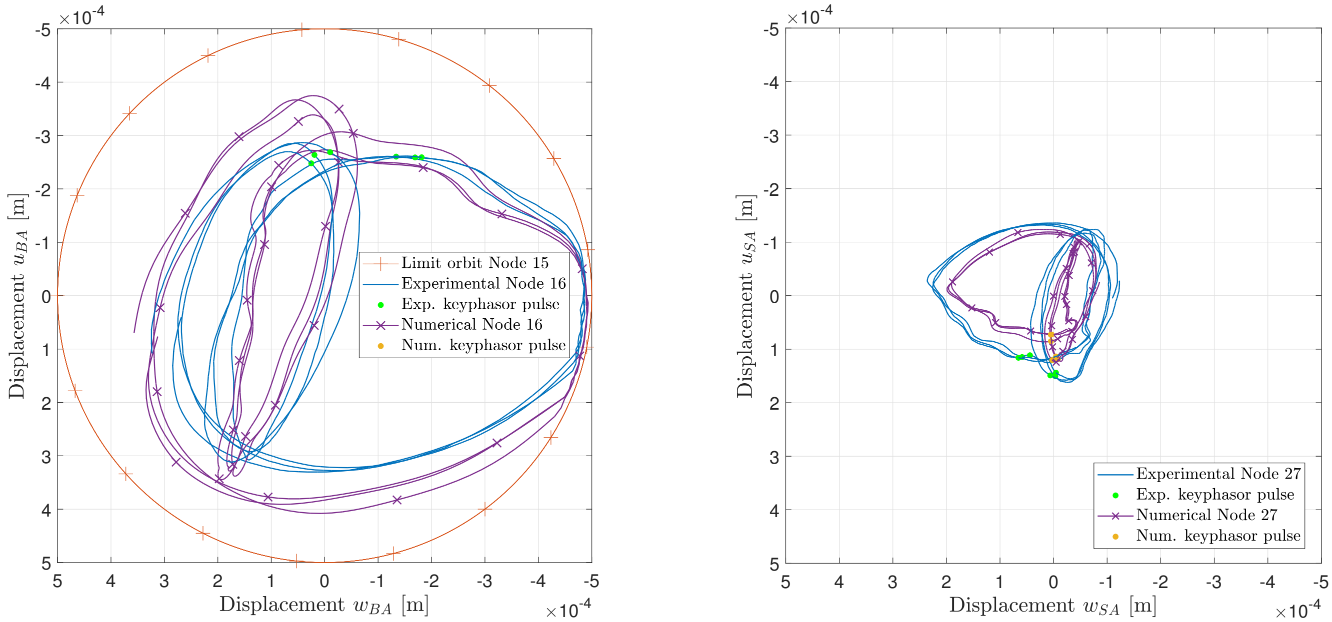

(a)

(b)

Figure 7. Predicted and measured shaft responses over 0.21 s (6 shaft revolutions) to a horizontal harmonic translational base motion, mass unbalances and rotor-stator contacts with $\dot{\phi}^* = 1700$ rpm: (a) Node 16 and (b) Node 27

Although these results are shown for an apparent steady state, it seems that the shaft response is not purely periodic but rather quasi-periodic. This can be attributed mainly to the rub-contact but also to the fact that the base excitation produced by the 6-DOF shaker is never perfectly constant and harmonic. In spite of this, the predicted and measured results match relatively well at both Nodes 16 and 27. In particular, the shaft impacts only the MCR within a small angular sector as seen in Fig. 7a, the period doubling due to the base excitation at

0.5X is well reproduced and the shaft positions at the keyphasor pulses are quite similar. Furthermore, although Node 27 is near the shaft free end and far from the MCR, the nonlinear deformation of its orbit induced by both the contact in the MCR and the journal bearings is clearly well predicted. The deviations in amplitude are similar to those observed in the previous fixed base analysis.

To complete these results, the full spectrums [30] of the orbits of Node 27 are computed and shown in Fig. 8. These spectrums are obtained from the response in quasi steady-state regime over a time interval of 1 s and are normalized by the signal length. The numerical-experimental agreement is now also demonstrated in the frequency domain. Besides, all the harmonics of 0.5X assigned to the nonlinearities are clearly visible. It is seen that while the peak at 1X corresponds to a forward whirl (amplitude of the +1X peak is higher than that of -1X) and consequently to the mass unbalance excitation, all the other harmonics are relatively both forward and backward and are thus related to the base translational excitation.

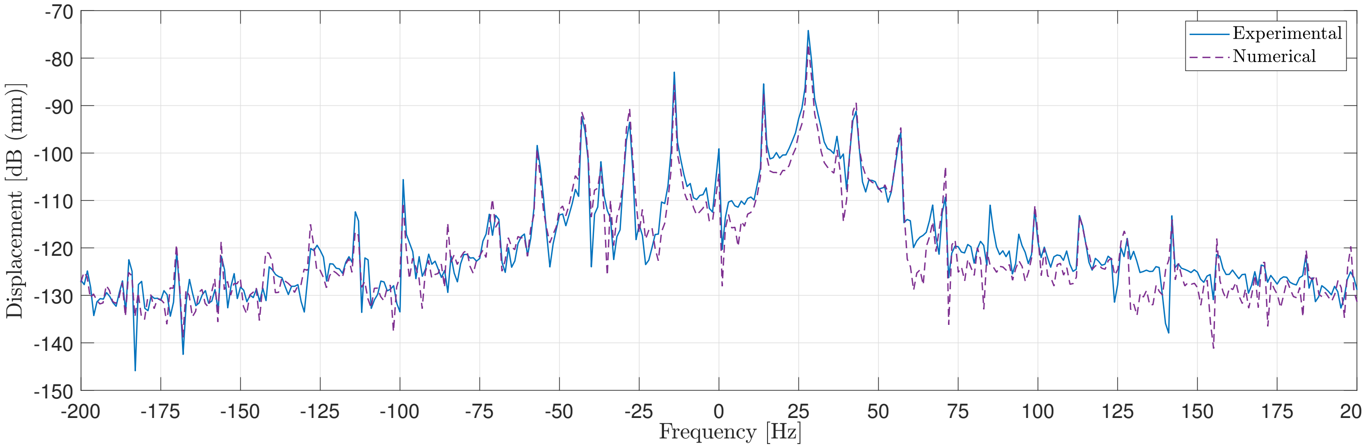

Figure 8. Full spectrums of the radial displacements of Node 27 in case of a horizontal harmonic translational base motion, mass unbalances and rotor-stator contacts with $\dot{\phi}^* = 1700$ rpm

3.4. Shock base excitation

In this section, base excitation with shock time profile is addressed. The aim of such excitation was to induce a dry-whip phenomenon in a similar way as hammer impact does. Moreover, unlike random excitation, shock excitation permits controlling efficiently the instant of time when the dry-whip is triggered and thus facilitating the correlation with the numerical predictions that require to adjust some parameters such as the friction coefficients. The targeted base motion (i.e. the motion that is aimed to be performed by the shaker) in this case comprises two transverse translational impulses of half-sine type with pre- and post-pulses defined in acceleration such as $\ddot{X}_{0,tr} = A_x f_{hs}(t, t_{x,0}, T_x, q)$ and $\ddot{Z}_{0,tr} = A_z f_{hs}(t, t_{z,0}, T_z, q)$ with A_x and A_z being the maximum amplitudes of the main impulse along $\vec{X}_0$ and $\vec{Z}_0$, respectively, and

$$f_{hs}(t, t_0, T, q) = \begin{cases} 0 & \forall t < t_1 \\ -q \sin\left(\pi \frac{t-t_1}{T_q}\right) & \forall t \in [t_1; t_2] \\ \sin\left(\pi \frac{t-t_2}{T}\right) & \forall t \in]t_2; t_3] \\ -q \sin\left(\pi \frac{t-t_3}{T_q}\right) & \forall t \in]t_3; t_4] \\ 0 & \forall t > t_4 \end{cases} \tag{4}$$

the shock function with half-sine series. The latter, represented in Fig. 9a, comprises three parameters: t_0 the instant corresponding to the maximum of the main impulse, T the width of the main impulse and q the amplitude of the pre- and post-impulses (always defined as 10 % in the sequel). The remaining variables are computed from these three parameters, such as $T_q = T/(2q)$, $t_1 = t_0 - T/2 - T_q$, $t_2 = t_0 - T/2$, $t_3 = t_0 + T/2$ and $t_4 = t_0 + T/2 + T_q$. The standard pre- and post-impulses are used in order to facilitate the driving process of the hydraulic shaker. An example of such an impulse is shown in Fig. 9b for the $\vec{X}_0$ direction.

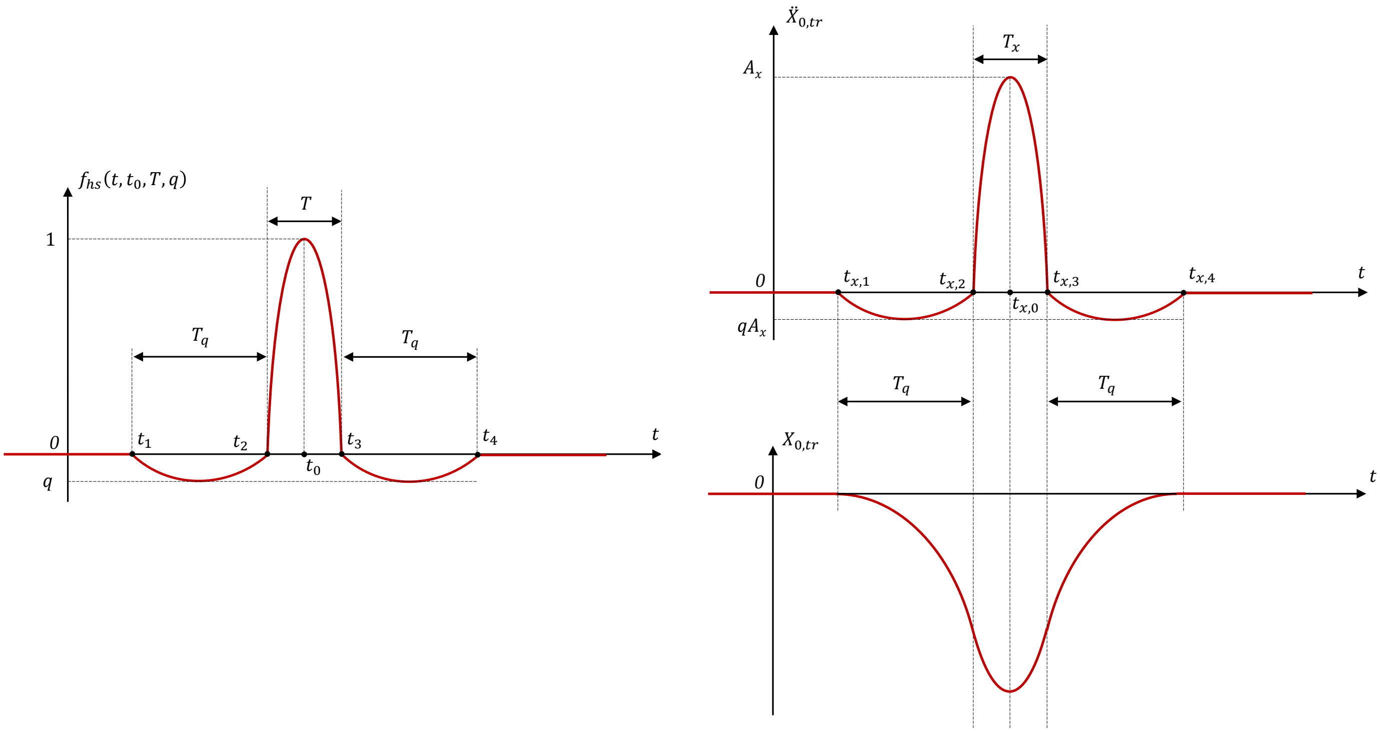

(a)

(b)

Figure 9. (a) Illustration of the half-sine series of the shock function $f_{hs}(t, t_0, T, q)$ and (b) Example of the acceleration and corresponding displacement in $\vec{X}_0$ with $\ddot{X}_{0,tr} = A_x f_{hs}(t, t_{x,0}, T_x, q)$

3.4.1. Experimental evidencing of the dry-whip

In this first test, the targeted base motion parameters are $A_x = 15$ m/s^2, $A_z = -15$ m/s^2 and $T_x = T_z = 10$ ms. The main impulses in the two directions are intended to be synchronous. By defining $t = 0$ s so that it corresponds to a keyphasor pulse in the steady-state mass unbalance response, the time $t_{x,0} = t_{z,0}$ of maximum shock accelerations in both directions turned to be 2.55 s. The targeted and real (experimental) DOFs of the rotor base are presented in Fig. 10. In Fig. 10b, the accelerations are plotted with a minus sign to evaluate the corresponding inertial forces (which are opposite to the accelerations) and the orientation of the axis is chosen to be the same as that of the orbits. The major difference between the targeted and real base motions lies on the time interval for $t > 2.6$ s for which, while the targeted base motion is to be nil, the rotor base undergoes in practice significant accelereration levels of the same amount as the impulses. These undesired base accelerations originated from the dry-whip phenomenon occurring in the rotor test bench as it will be demonstrated in the following. This means that the vibration level in place was so important that the shaker's hydraulic pressure was not high enough to prevent the shaker's housing from moving (in the rigid-body sense). Owing to these discrepancies and as mentioned in Section 3.1, the real base motions were introduced in the FEM instead of the targeted ones to enhance the prediction of the dynamic behavior of the system.

The experimental response of the shaft to the base excitations and to the mass unbalances is first presented in Fig. 11 in terms of the eccentricities e_B (with respect to the center of the MCR) at Node 16, and e_S at Node

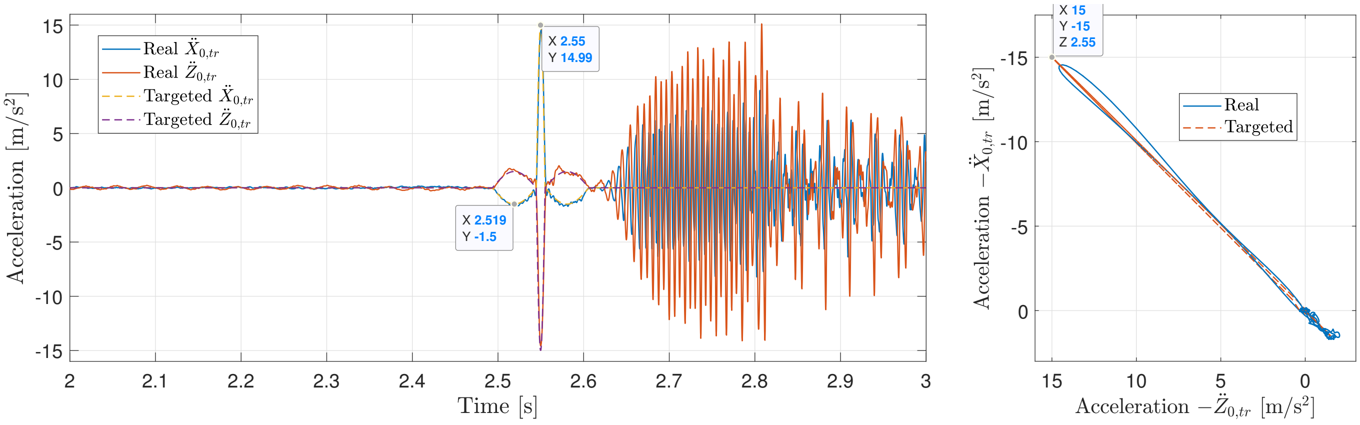

(a) (b)

Figure 10. Transverse translations of the rotor base for the first study case in shock excitation: (a) with respect to time and (b) orbit in [0;2.616] s

27. Analyzing the eccentricity rather than the two shaft transverse displacements permits assessing both the displacements with only one signal, determining quickly if contacts occur, and having a better insight of when the dry-whip starts. The dry-whip is firstly evidenced by the very sudden rise of the eccentricities that occurred for $t \in [2.55; 2.668]$ s. These eccentricities reached a more stable state afterwards for $t \in [2.668; 2.804]$ s and then significantly oscillated for $t \in [2.804; 3]$ s. These oscillations will be explained in the next section. After $t > 3$ s, the motor-shaft coupling was suddenly broken as due to the considerable shaft displacements. The dry-whip entered then into a relatively stable state for $t > 3.5$ s which was maintained until the shaft coasted down to a sufficiently low value where the dry-whip vanished for $t > 6$ s. Lastly, it must be highlighted that the eccentricity of Node 16 could exceed the clearance c_b of the MCR since the shaft in dry-whip underwent not only high transverse displacements but also high transverse rotations. This will be further shown in the next section.

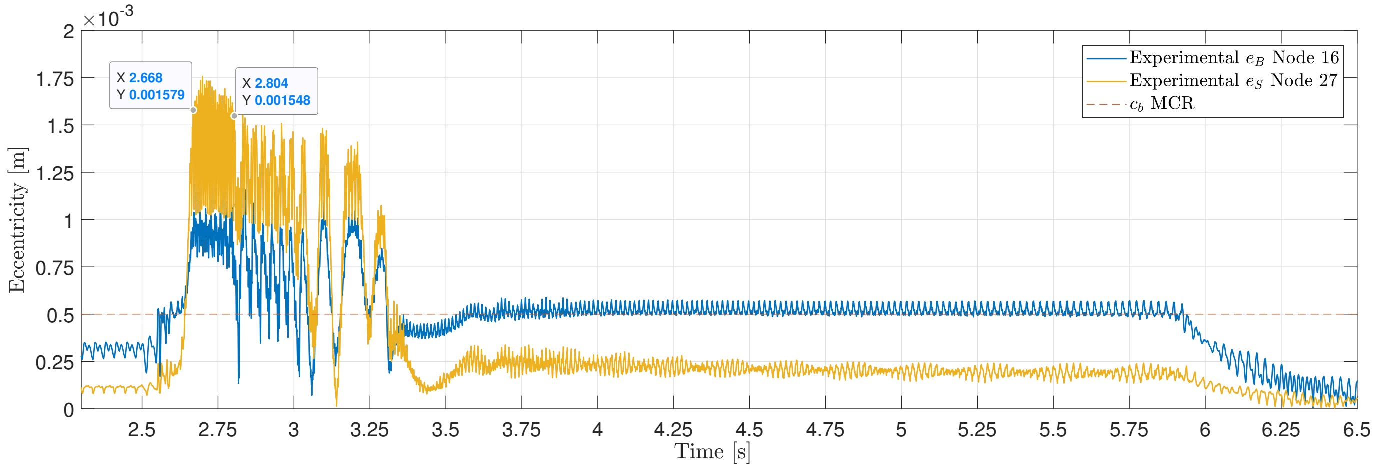

Figure 11. Experimental response of the shaft to mass unbalances and to the shock excitation of Fig. 10 with $\dot{\phi}^* = 1700$ rpm

The full spectrogram [30] of the complex displacement $w_{BA} + iu_{BA}$ of Node 16 is computed and plotted in Fig. 12. This result illustrates clearly the whirl change occurring after the main impulse: before $t = 2.55$ s, the rotor presented mainly a forward whirl with a frequency 1X related to the mass unbalances only while after $t = 2.55$ s it turned into a backward whirl with a characteristic negative frequency yielding up to -170 Hz in the transient part. Then, the whirl still remained backward, however the frequencies slowly decreased with a quite constant eccentricity (as in Fig. 11) until $t \approx 6.5$ s.

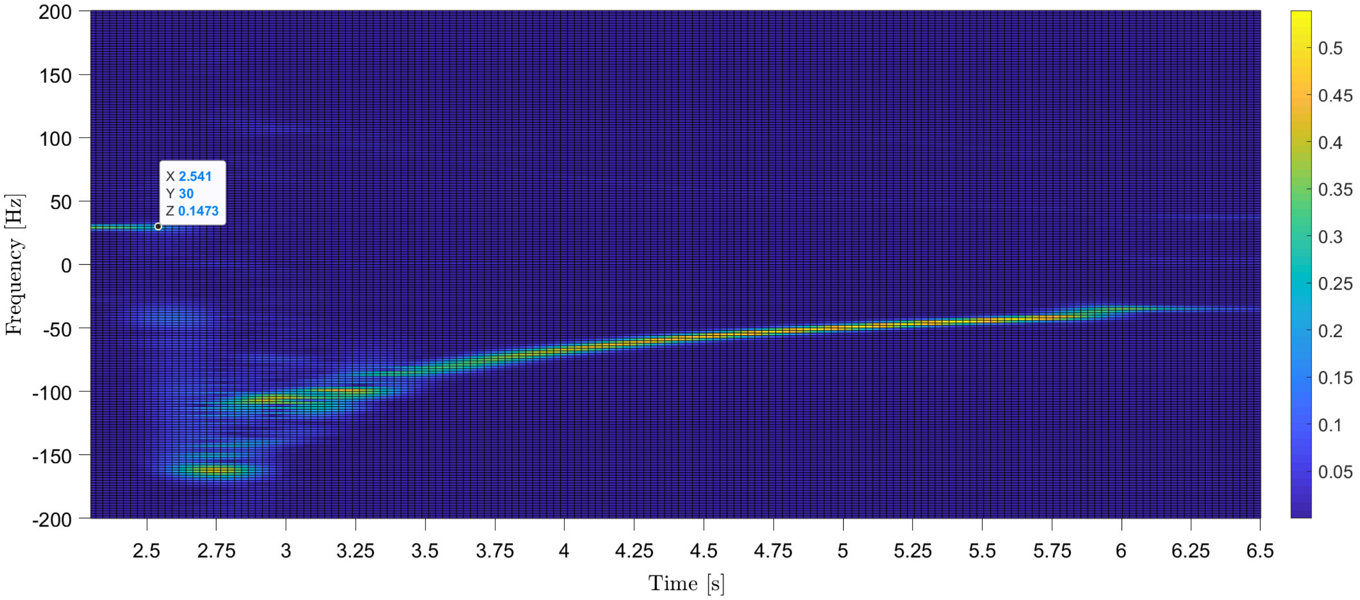

Figure 12. Experimental full spectrogram corresponding to the eccentricity e_B of Node 16 of Fig. 11 with $\dot{\phi}^* = 1700$ rpm (the color bar amplitudes are in dB/Hz)

In order to confirm one last time that this dynamic behavior was indeed a dry-whip, a video performed with a high-frequency camera providing a frame-rate of 2000 fps (frame-per-second) is available from Appendix A. This video shows the free end of the shaft during this test, in which the support of the axial sensor was removed (the second radial sensor support at Node 27 can be seen around the shaft) and the camera was pointed toward the motor as for the orientation of Fig. 2a. A slow motion was performed by reducing the frame rate from 2000 fps to 24 s which means that one second in reality corresponds to $2000/24 \approx 83.3$ s in the video. In this context, the video approximately corresponds to the experimental time interval $t \in [2.1; 4.0]$ s. Thus, in the interval [0-30] s of this video the forward whirl is identified with small transverse displacements. In the interval [30-34] s occurs the shock from the base which moves in translation all the elements fixed to the shaker's housing, including the hydrodynamic bearings that support the rotor shaft. After 34 s, the transitions to backward whirl and the dry-whip with considerable amplitudes and frequencies are clearly observed. The high oscillations of the shaft eccentricity of Node 27 shown in Fig. 11 for $t \in [3; 3.5]$ s can also be noticed.

3.4.2. Experimental validation of the model and numerical investigations

In this section, it is demonstrated that the dry-whip that was shown experimentally in the previous section can be accurately predicted with the numerical model described in Section 2. To this aim, the eccentricities e_B at Node 16 and e_S at Node 27 are compared experimentally and numerically for several values of the friction coefficient μ of the MCR in Fig. 13, with a focus on the transient state. Comparison after $t = 3$ s is not addressed since the model is no longer valid once the motor-shaft coupling was broken. The result with the model which does not consider the SCRs is also shown. It is noted that the model succeeds to reproduce in any case the occurrence of the dry-whip phenomenon. The first time instants after the impulse are quite similar. Nonetheless, the numerical results differ rapidly depending on μ when the dry-whip starts to take place after $t > 2.6$ s. In particular, the value of $\mu = 0.39$ seems to be the best choice at both Nodes 16 and 27 for the experimental and numerical results to present a synchronous increase. If the SCRs are not considered, it is shown that the shaft displacements keep on increasing until very significant values, which are much higher than the experimental ones. In contrast, with the SCRs, the dry-whip sudden increase is quickly stopped for $t \approx 2.67$ s. The numerical eccentricities are then much closer to the experimental ones. In addition, the high oscillations of eccentricities occurring experimentally at Node 16 for $t > 2.8$ s are also observed numerically; however, for earlier time values. This may be explained by the fact that the dynamics taking place is highly nonlinear and thus depends strongly on both the initial conditions at the shock impulse and the contact parameters. For example, it can be seen that the experimental eccentricity at Node 16 already exceeds the clearance c_b at $t = 2.55$ s, which means that the experimental clearance may be higher than expected. Moreover, the contact parameters of the SCRs are not as controlled as those of the MCR and there might exist better values than those that have been adjusted, as shown in Table 5.

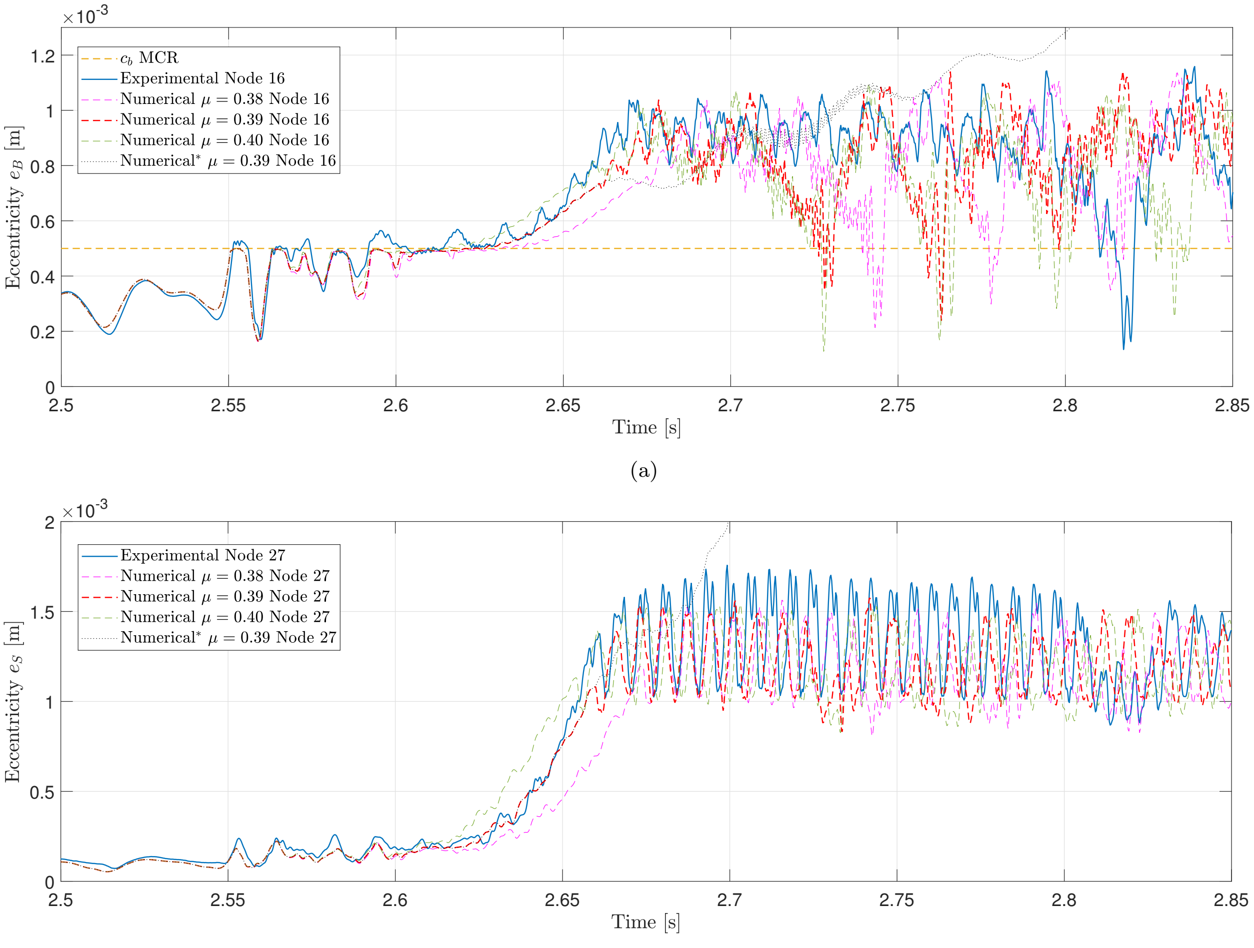

(a)

(b)

Figure 13. Predicted and measured shaft eccentricities in response to mass unbalances and to the shock excitation of Fig. 10 with $\dot{\phi}^* = 1700$ rpm (the notation * corresponds to the model for which the SCRs are not considered): (a) Node 16 and (b) Node 27

The shaft orbits of Nodes 16 and 27 are presented in Fig. 14, with $\mu = 0.39$ for the numerical curves. The full spectrums are not shown since the transient state is too short to obtain a reasonable frequency resolution. The experimental-numerical agreement is once again noteworthy, either before or after the shock impulse (whose effect on the shaft orbit agrees with the direction of the accelerations shown in Fig. 10b). In particular, the transition between the forward and backward whirl is clearly identified simultaneously both experimentally and numerically at Node 16 about $t = 2.554$ s, although the contact point is not exactly at the same angular position on the MCR. Once again, it is noted that the experimental orbit at Node 16 exceeds the clearance c_b

of the MCR unlike the numerical one. Nevertheless, this is more obvious at other angular positions, e.g. for $t = 2.573$ s. This means that the MCR may in fact not be perfectly circular instead of having an overall higher clearance, as it will be demonstrated in Section 3.4.3. The important shaft transverse rotations could also be incriminated, as mentioned in Section 3.4.1, however this seems less likely since the numerical orbit never exceeds the limit orbit for this time interval. Regarding Node 27 in Fig. 14b, the experimental and numerical orbits are relatively close, even in the transient state where the eccentricities suddenly grow and in the more stable state for $t > 2.661$ s. It must be pointed out that this stable orbit for $t > 2.661$ s presents a center which is shifted horizontally, i.e. in w_{SA}, with respect to the center of the stable orbit for $t < 2.55$ s. This shift was reproduced numerically by imposing a horizontal offset in the position of the center B of the SCR9 as given in Table 5. Likewise, the clearance of the SCR9 had to be increased so as to retrieve a similar eccentricity of the experimental orbit for $t > 2.661$ s. This SCR and its parameters were chosen to be adjusted numerically since, according to the model, it is the second ring after the MCR to experience rotor-stator contacts (for $t > 2.660$ s) and to show the most important normal contact forces. The model also predicted contacts in the SCRs 1 (for $t > 2.695$ s), 4 (for $t > 2.717$ s), 6 (for $t > 2.723$ s) and 7 (for $t > 2.667$ s) whose RMS normal forces on $t \in [0; 3]$ s are 109 N, 388 N, 87 N, 176 N, respectively, while they are of 329 N for the MCR and 476 N for the SCR9.

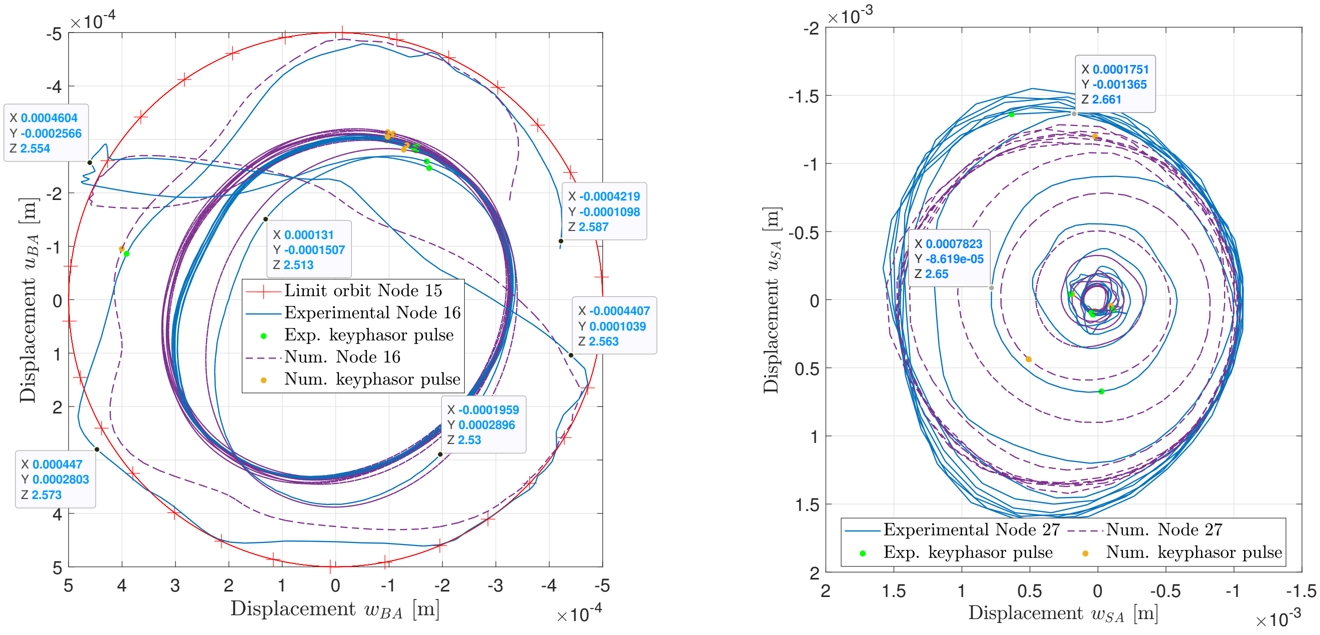

(a)

(b)

Figure 14. Predicted and measured shaft orbits in response to mass unbalances and to the shock excitation of Fig. 10 with $\dot{\phi}^* = 1700$ rpm: (a) Node 16 for $t \in [2.2; 2.587]$ s and (b) Node 27 for $t \in [2.2; 2.71]$ s

Given that the model can now be considered realistic, the deformed shape of the shaft in bending during the dry-whip can be assessed numerically. Therefore, the results shown in Fig. 15 are computed for three time instants: before the shock excitation at $t = 2.5$ s; during the transient increase of the dry-whip when there was no contact in the SCRs yet at $t = 2.65$ s; when the dry-whip was relatively stable and before the motor-shaft coupling was broken at $t = 2.85$ s. The deformed shapes are presented accounting for the quasi-static deformed shape associated to the gravity load. Moreover, the MCR and the five SCRs subject to contacts are plotted, considering their center's offset (only in $\vec{x}$ for Fig. 15a). From Fig. 15a, it can be seen, as expected, that before the shock base excitation the shaft deforms due to the mass unbalances on its first mode and that there is no phase shift between the bending DOFs of each node (blue straight line in the section view of Fig. 15b).

On the contrary, for $t = 2.65$ s, the shaft adopts a new deformed "W"-shape owing to the permanent contact with the MCR. In addition, the bending DOFs of each node started to present a phase shift, which induces a deformed shape in the $x - z$ plane. This can be assigned to the sudden acceleration of the backward whirl at the MCR that is not instantly transmitted to the shaft ends. At $t = 2.85$ s, the deformed "W"-shape turns into a deformed "N"-shape owing to the contacts in the SCRs 1, 4, 6, 7 and 9. These new contacts tend to accelerate or decelerate the shaft backward whirls in different ways depending on the contact node. For instance, the sliding speed is mainly negative in the SCRs 6 and 7 owing to the higher clearance and consequently higher eccentricities, while it is mainly positive in the MCR and the others SCRs. Then, the phase shift between the bending DOFs of each node is even more pronounced. Furthermore, the transverse rotations are significative, in particular at the MCR, which explains why the eccentricities at Node 16 exceeded the MCR clearance in Fig. 13a and Fig. 11. On the other hand, the large transverse displacements at Node 1 were probably the reason for the failure of the motor-shaft coupling.

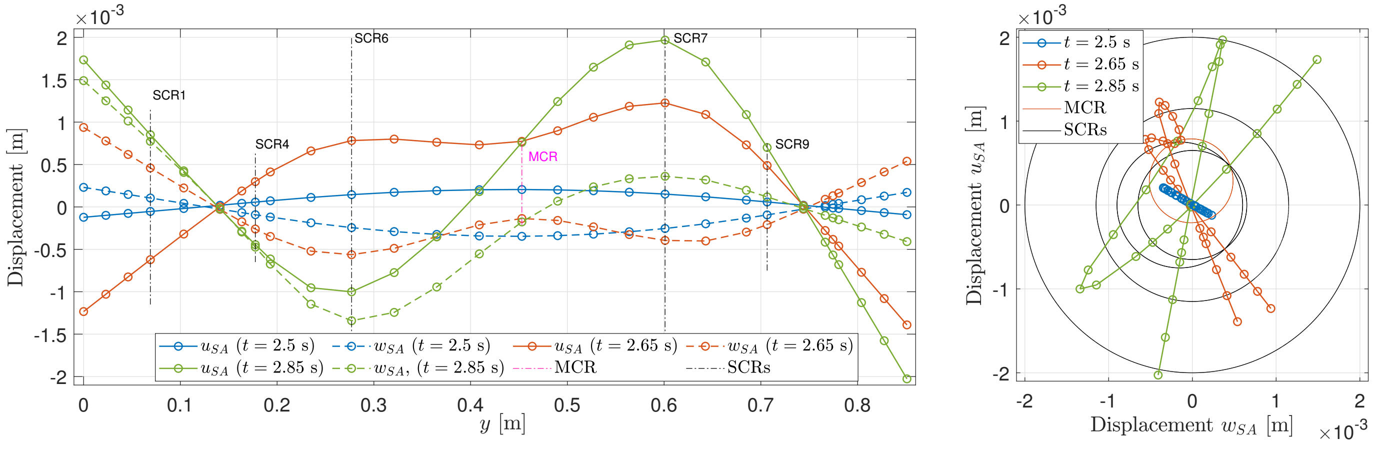

(a) (b)

Figure 15. Computed deformed shape of the shaft at different time instants with $\dot{\phi}^* = 1700$ rpm: (a) with respect to y and (b) section view

Another source of the motor-shaft coupling's failure may also be the torsion to which it was subject. To this aim, the torsional displacement β of Node 1 with respect to time is shown in Fig. 16a. Moreover, a photograph of the coupling at failure (in a different test) is presented in Fig. 16b. According to the model, the coupling was also deformed with large amplitudes on its first torsional mode of frequency ≈ 10.4 Hz (which is a rigid-body mode of the shaft with deformation only in the coupling [31]) due to the high axial friction moment acting in the MCR. The negative sign of the torsion is explained by the direction of the tangential friction force which is opposite to the sliding speed in the MCR. These oscillations create an oscillation of ± 50 rpm of the actual shaft speed of rotation of $\phi^* = 1700$ rpm. By looking at Fig. 16b, the torsion can be highlighted at the failure by the phase shift between the two screws (that tighten the motor and the shaft) which should normally be perfectly aligned.

The measured axial displacement was also found to be important, i.e., about ± 2 mm at ≈ 4 Hz (which is the rigid-body mode of the shaft with deformation only in the coupling [31]). Nonetheless, this was not matching with the model which predicted displacements around ± 25 µm only. This deviation can be assigned to the existence of some coupling between torsional and axial displacements in the motor-shaft coupling, which was not characterized experimentally and for this reason was not introduced in the model.

3.4.3. Influence of non-synchronous orthogonal shocks on the dry-whip occurrence

The objective here is to show the influence on the dry-whip triggering when imposing a time delay between the two transverse base translations. This time delay affects the instantaneous direction of the base translation

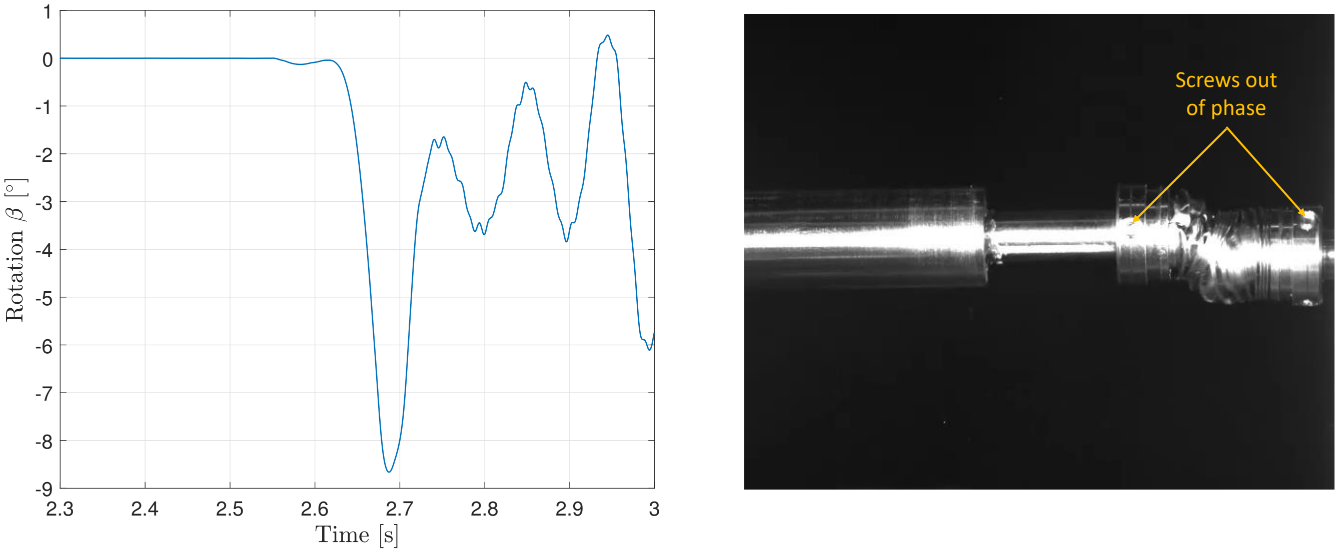

(a)

(b)

Figure 16. Deformation of the motor-shaft coupling in torsion with $\dot{\phi}^* = 1700$ rpm: (a) computed variation with respect to time and (b) photograph at the failure

which becomes multi-axial. In particular, it is possible with this parameter to favor a forward whirl of the shaft instead of the dry-whip's typical backward whirl. In this context, the same two transverse base shocks as defined in Eq. (4) were imposed to the test bench, however with a time delay between the two directions $\vec{X}_0$ and $\vec{Z}_0$. The parameters were then $A_x = 15$ m/s^2, $A_z = -15$ m/s^2, $T_x = T_z = 10$ ms, and a time delay of $t_{z,0} - t_{x,0} = 0.0049$ ms. An example of such targeted vs real (experimental) base motion is presented in Fig 17. From Fig 17b, it is clear that the multi-axial inertial forces related to these base accelerations favored the forward whirl of the shaft, in contrast to the synchronous base accelerations of Fig. 10b which resulted in a straight uniaxial inertial force without whirl.

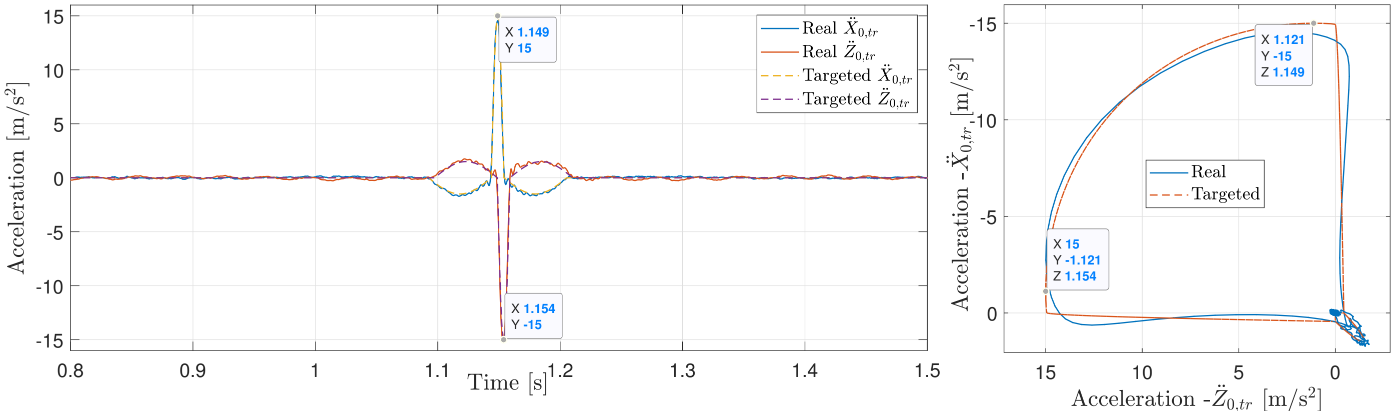

(a)

(b)

Figure 17. Rotor base motion for the shock excitation case with two non-synchronous transverse translations: (a) with respect to time and (b) orbit

During 15 minutes, a burst shock was carried out every 10 s, high enough to get a novel steady state and not a multiple of the speed of rotation in order to vary the shaft angular position contact with the MCR. The measured response of the shaft at Node 16 in terms of u_{BA} and w_{BA} with respect to the MCR is presented in Fig. 18. Firstly, no dry-whip was observed for the 90 impulses generated. The shaft always impacted the MCR only and returned rapidly to its steady state in response to the mass unbalances. From Fig. 18b, it can be highlighted that every angular position of the MCR was indeed impacted. Besides, by superimposing the limit orbit of the MCR clearance on the shaft orbit, the non-circularity of the ring can be identified, which justifies the exceeded clearance of the experimental shaft orbit observed in Fig. 14a.

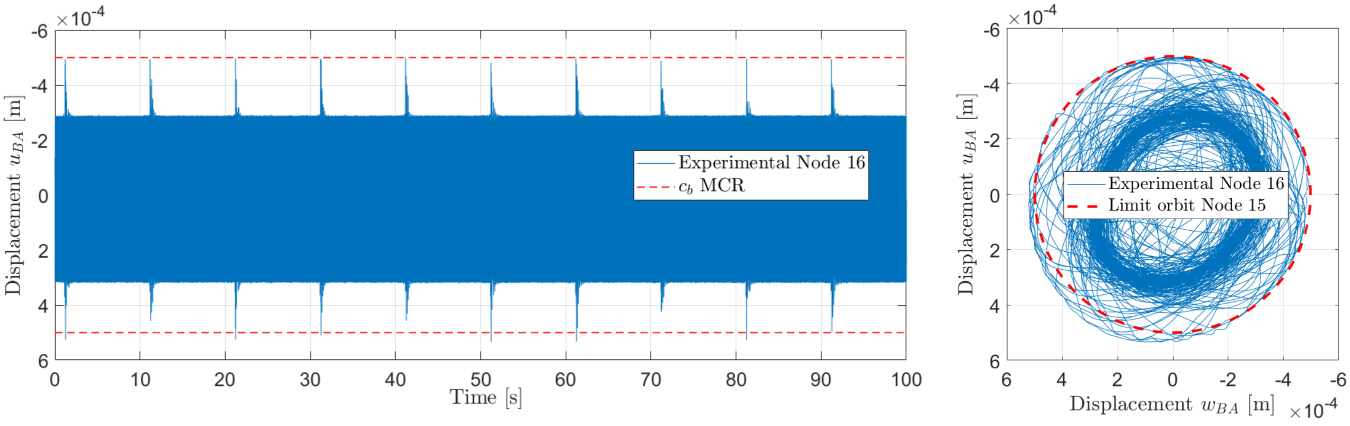

(a)

(b)

Figure 18. Measured response of the rotor on the first 100 s to two non-synchronous transverse base shocks repeated every 10 s over 15 min with $\dot{\phi}^* = 1700$ rpm: (a) with respect to time and (b) shaft orbit

In order to confirm that the dry-whip was indeed inhibited by the delay between the two base translational shocks, the numerical shaft response at Node 16 corresponding to the excitation of Fig. 17 is computed and compared to the experimental one in Fig. 19. The friction coefficient used for the MCR was maintained as $\mu = 0.39$. It can be seen that the model also predicts no dry-whip with a progressive return to the mass unbalance steady-state. Regarding the numerical-experimental correlation, the first time instants during the impulse show a satisfactory agreement. The predictions of the model in the transient period after $t > 1.25$ s and before the return to the steady state are less accurate, with higher calculated amplitudes as in Fig. 7a. This deviation cannot be assigned to the friction coefficient which does not have much influence here but rather to an underestimation of the real rotor bending stiffness, maybe due to the restricted assumptions of the journal bearing modelling.

3.4.4. Influence of the base shock amplitude on the dry-whip occurrence

The aim of this section is to analyze if the amplitude of the base motion used in Section 3.4.3 has an influence on the dry-whip occurrence. Thus, the amplitudes were arbitrarily doubled. The parameters of the shock were then $A_x = 30$ m/s^2, $A_z = -30$ m/s^2, $T_x = T_z = 10$ ms, and a time delay of $t_{z,0} - t_{x,0} = 0.0049$ ms. Once again, the shocks were repeated several times, independently of the shaft angular position. The dry-whip was successfully triggered after the fifth impulse. The predicted and measured responses of the shaft to this fifth impulse are presented in Fig. 20. The corresponding time instant of maximum acceleration along $\vec{X}_0$ is $t_{x,0} = 1.662$ s. Therefore, it can be inferred that the amplitude of the base shocks can indeed influence the occurrence of the dry-whip, despite the time delay between the two base translational shocks which favors the forward whirl. Nevertheless, the shaft angular position on its orbit related to the mass unbalances when the impact is generated has also a great influence since the dry-whip only occurred at the fifth impulse. The model with a coefficient of friction $\mu = 0.39$ and $\mu = 0.40$ in the MCR permitted obtaining the same conclusion as with the experiment, which emphasizes the experimental outcomes of this section.

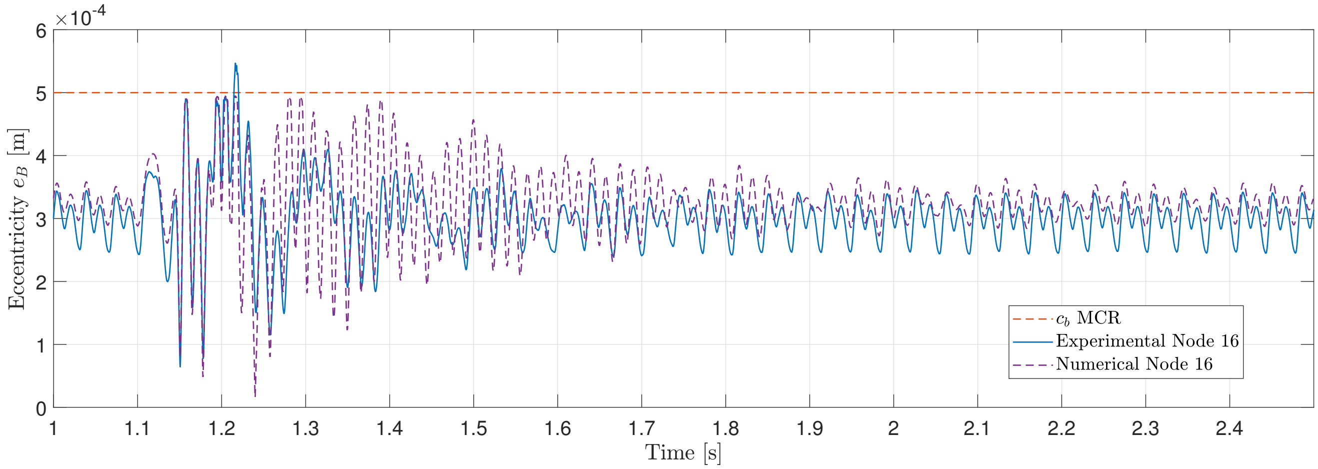

Figure 19. Predicted and measured responses of the rotor to the two non-synchronous transverse base shocks of Fig. 17 with $\dot{\phi}^* = 1700$ rpm

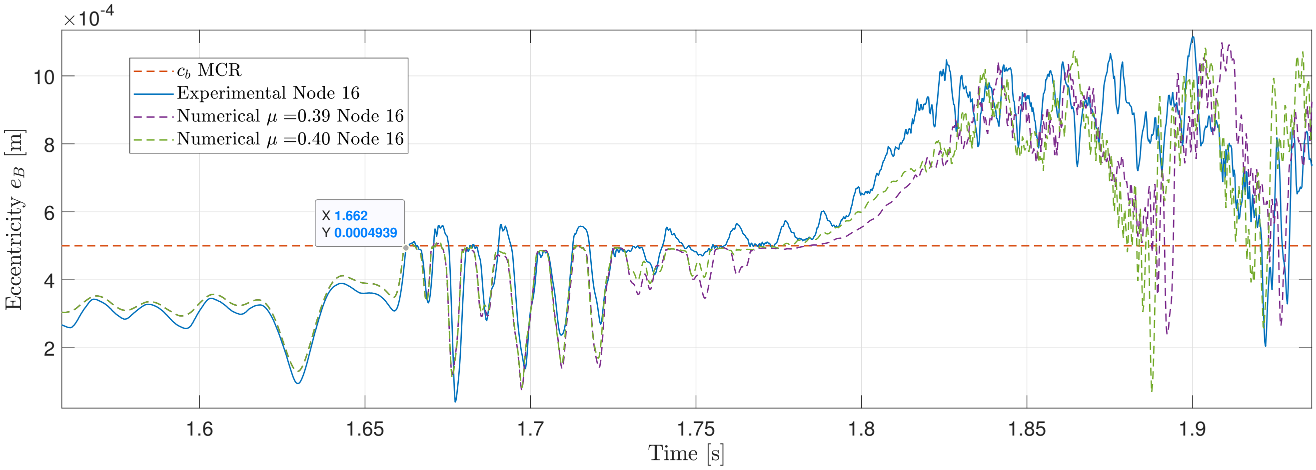

Figure 20. Predicted and measured responses of the rotor to two non-synchronous transverse base shocks with higher amplitudes and $\dot{\phi}^* = 1700$ rpm

4. DISCUSSION

The test bench under study is relatively flexible with a small shaft diameter/length ratio and a low stiffness motor-shaft coupling, and highly mass unbalanced. This specific design was intended to demonstrate efficently by experiments the contact phenomena and their harmful consequences such as the dry-whip, and to provide a proper experimental validation of the associated numerical model that was developped.

The dry-whip was successfully triggered from base excitation and clearly identified by measurements, high-frequency camera and numerical calculations. It was shown that the base motion direction may have a great impact on triggering the instability, depending on how it favors the shaft orbit whirl at the contact. The angular position of the shaft on its orbit at the main impulse, and consequently the angle of contact, has also a great influence as it was pointed out by Bartha [32]. In practice, the trigerring of the dry-whip was found to be quite reproductible, especially for the two synchronous translational shocks from the base. Nevertheless, a progressive wear was noticed at the two contact surfaces of the shaft and the MCR, which tended to increase the dry-friction coeffcient and thus to facilitate more and more the dry-whip occurrence. The instability was also observed with random base translations with small amplitude (maximum accelerations up to 0.3 g), but the wear was too pronounced for the results to be compared with the shock excitation case.

In regards to the experimental and numerical comparisons, some deviations were noticed and can be mainly assigned to the following reasons:

- The limitations of the hydrodynamic bearing modelling assumptions, which do not include the temperature variations inside the oil-film, the viscosity variations with temperature and pressure, the effect of rugosity for high eccentricities, etc. More reliable numerical calculations were conducted with pressure fields obtained from a FEM solving accounting both for the finite-length geometry of the journal bearings and for cavity problems (using Reynolds boundary conditions), however the results were similar to those obtained with the short-bearing hypothesis and the Gümbel boundary conditions.
- The imperfect circular shape of the MCR of the test bench.
- The experimental uncertainties such as in the contact parameters of the SCRs, a residual unbalance stemming from an imperfect rotor balancing, a non-measured shaft run-out which can reveal to be quite important for this shaft diameter/length ratio, the motor-shaft coupling characteristics that may differ from those specified by the manufacturer (and the existence of some off-diagonal coefficients coupling the bending, torsion and axial effects), and a likely radial misalignement between the journal bearing centers.

5. CONCLUSION

In the present paper, dry contacts directly between the shaft and circular stator parts were addressed, which can be representative of the likely contacts occurring for instance in power plant turbo generators with contact on the generator side or in compressors mounted on foil bearings, although these examples may have lower stator stiffness values than those in the present paper. These contacts originated here from the base excitations as due to the on-board feature of the rotor, which also belong to the wide range of excitations experienced by such turbomachines used in the aerospace, aeronautics and energy industries. The effect of the shaft-stator rub on on-board rotordynamics has been simulated both numerically and experimentally. The proposed numerical model was able to predict with great accuracy the contact dynamics originated from transverse translational base motions. This was achieved despite the limitations of the hydrodynamic bearing modelling which used the short-bearing hypothesis and applied the Gümbel boundary conditions. The model was first validated in the case of a fixed base with mass unbalance excitation only, providing a good insight of the influence of the hydrodynamic bearing nonlinearities. It was then validated in both time and frequency domains in the case of harmonic base transverse translations inducing an unilateral contact.

The dry-whip instability was evidenced both experimentally and numerically with the shock base translations, in terms of shaft eccentricities, shaft orbits and full spectrogram. It was demonstrated that contacts occurred not only at the middle of the shaft (MCR) but also at several other axial locations (SCRs) owing to the considerable amplitudes of displacement involved during the dry-whip. The latter was responsible for the rapid failure of the motor-shaft coupling, preventing from converging towards a steady-state behavior in backward whirl. Besides, high oscillations of the shaft eccentricities related to the multiple contacts in the SCRs were also calculated. The model permitted assessing the operational deformed shape of the shaft during the instability, which exhibited the high transverse displacements and rotations, and the phase shift between the bending DOFs caused by the high tangential friction forces. Finally, it was shown, as expected, that a multi-axial base motion favoring a forward whirl tended to inhibit the occurrence of the dry-whip. However, it was still possible to trigger it in this case by doubling the base motion amplitude. Then, it would be of great interest to perform numerical multi-parametric studies to find the exact boundaries of the dry-whip existence domain, depending on all the base motion parameters.

Acknowledgements

This work was supported by the French National Research Agency (ANR) in the framework of ANR-Labcom-SME AdViTAM, 16-LCV1-0006 and Equipex PHARE 10-EQPX-0043. The authors are also thankful to the scholarhip provided by CAPES-Print project (Brazil).

CRediT authorship contribution statement

Yvon Briend: Conceptualization, Formal analysis, Investigation, Methodology, Software, Validation, Visualization, Writing - original draft. **Eric Chatelet:** Conceptualization, Funding acquisition, Investigation, Project administration, Resources, Supervision, Writing - original draft. **Régis Dufour:** Conceptualization, Funding acquisition, Investigation, Resources, Supervision, Writing - original draft. **Marie-Ange Andrianoely:** Software. **Franck Legrand:** Investigation, Validation, Resources. **Marcelo Samora Sousa Jr:** Methodology. **Valder Steffen Jr:** Funding acquisition, Supervision, Writing - original draft. **Sophie Baudin:** Funding acquisition, Project administration.

Declaration of Competing Interest

None.

References

[1] H. Black, Interaction of a whirling rotor with a vibrating stator across a clearance annulus, Journal of Mechanical Engineering Science 10 (1) (1968) 1–12.

[2] A. Lingener, Experimental investigation of reverse whirl of a flexible rotor, in: Proceedings of 3rd International Conference on Rotor dynamics,(1990-9), 1990.

[3] D. E. Bently, J. J. Yu, P. Goldman, A. Muszynska, Full annular rub in mechanical seals, part i: experimental results, International Journal of Rotating Machinery 8 (5) (2002) 319–328.

[4] D. E. Bently, P. Goldman, J. J. Yu, Full annular rub in mechanical seals, part ii: Analytical study, International Journal of Rotating Machinery 8 (2002).

[5] Y. Choi, Investigation on the whirling motion of full annular rotor rub, Journal of Sound and Vibration 258 (1) (2002) 191–198.

[6] D. W. Childs, A. Bhattacharya, Prediction of dry-friction whirl and whip between a rotor and a stator, J. Vib. Acoust. 129 (3) (2007) 355–362.

[7] J. C. Wilkes, D. W. Childs, B. J. Dyck, S. G. Phillips, The numerical and experimental characteristics of multimode dry-friction whip and whirl, Journal of Engineering for Gas Turbines and Power 132 (5) (2010).

[8] J. Jiang, Determination of the global responses characteristics of a piecewise smooth dynamical system with contact, Nonlinear Dynamics 57 (3) (2009) 351–361.

[9] G. Jacquet-Richardet, M. Torkhani, P. Cartraud, F. Thouverez, T. N. Baranger, M. Herran, C. Gibert, S. Baguet, P. Almeida, L. Peletan, Rotor to stator contacts in turbomachines. review and application, Mechanical Systems and Signal Processing 40 (2) (2013) 401–420.

[10] H. Ma, F. Yin, Y. Guo, X. Tai, B. Wen, A review on dynamic characteristics of blade–casing rubbing, Nonlinear Dynamics 84 (2) (2016) 437–472.

[11] K. Prabith, I. P. Krishna, The numerical modeling of rotor–stator rubbing in rotating machinery: a comprehensive review, Nonlinear Dynamics (2020) 1–47.

[12] J. Hong, P. Yu, D. Zhang, Y. Ma, Nonlinear dynamic analysis using the complex nonlinear modes for a rotor system with an additional constraint due to rub-impact, Mechanical Systems and Signal Processing 116 (2019) 443–461.

[13] Y. Pingchao, M. Yanhong, H. Jie, C. Guo, Application of complex nonlinear modes to determine dry whip motion in a rubbing rotor system, Chinese Journal of Aeronautics (2020).

[14] D. Laxalde, F. Thouverez, Complex non-linear modal analysis for mechanical systems: Application to turbomachinery bladings with friction interfaces, Journal of sound and vibration 322 (4-5) (2009) 1009–1025.

[15] S. Wang, L. Hong, J. Jiang, Characteristics of stick-slip oscillations in dry friction backward whirl of piecewise smooth rotor/stator rubbing systems, Mechanical Systems and Signal Processing 135 (2020) 106387.

[16] M. Behzad, M. Alvandi, Friction-induced backward rub of rotors in non-annular clearances: Experimental observations and numerical analysis, Tribology International 152 (2020) 106430.

[17] U. Ehehalt, O. Alber, R. Markert, G. Wegener, Experimental observations on rotor-to-stator contact, Journal of Sound and Vibration 446 (2019) 453–467.

[18] V. Srinivasan, A. Soni, Seismic analysis of a rotor-bearing system, Earthquake engineering & structural dynamics 12 (3) (1984) 287–311.

[19] Y. Hori, T. Kato, Earthquake-induced instability of a rotor supported by oil film bearings, J. Vib. Acoust. 112 (2) (1990) 160–165.

[20] L. Hou, Y. Chen, Q. Cao, Nonlinear vibration phenomenon of an aircraft rub-impact rotor system due to hovering flight, Communications in Nonlinear Science and Numerical Simulation 19 (1) (2014) 286–297.

[21] T. Gao, S. Cao, L. Hou, Y. Hou, An experimental study on the nonlinear vibration phenomenon of a rotor system subjected to barrel roll flight and coupled rub-impact faults, Measurement 153 (2020) 107406.

[22] C. Jarroux, J. Mahfoud, R. Dufour, F. Legrand, B. Defoy, T. Alban, Investigations on the dynamic behaviour of an on-board rotor-amb system with touchdown bearing contacts: modelling and experimentation, Mechanical Systems and Signal Processing 159 (2021) 107787.

[23] Y. Su, Y. Gu, P. S. Keogh, S. Yu, G. Ren, Nonlinear dynamic simulation and parametric analysis of a rotor-amb-tdb system experiencing strong base shock excitations, Mechanism and Machine Theory 155 (2021) 104071.

[24] C. A. Fonseca, I. F. Santos, H. I. Weber, Experimental comparison of the nonlinear dynamic behavior of a rigid rotor interacting with two types of different radial backup bearings: Ball & pinned, Tribology International 119 (2018) 250–261.

[25] Y. Briend, M. Dakel, E. Chatelet, M.-A. Andrianoely, R. Dufour, S. Baudin, Effect of multi-frequency parametric excitations on the dynamics of on-board rotor-bearing systems, Mechanism and Machine Theory 145 (2020) 103660.

[26] G. B. DuBois, F. W. Ocvirk, Analytical derivation and experimental evaluation of short-bearing approximation for full journal bearing (1953).

[27] P. Flores, J. P. Claro, J. Ambrósio, Journal bearings subjected to dynamic loads: the analytical mobility method, Revista da Associação Portuguesa de Análise Experimental de Tensões ISSN 122 (2006) 922.

[28] C. Duran, L. Manin, M.-A. Andrianoely, C. Bordegaray, R. Dufour, Effect of rotor-stator contact on the mass unbalance response, in: 9th IFToMM International Conference on Rotor Dynamics, 2014.

[29] Q.-T. Tran, K.-L. Nguyen, L. Manin, M.-A. Andrianoely, R. Dufour, M. Mahjoub, S. Menand, Nonlinear dynamics of directional drilling with fluid and borehole interactions, Journal of Sound and Vibration 462 (2019) 114924.

[30] P. Goldman, A. Muszynska, Application of full spectrum to rotating machinery diagnostics, Orbit 20 (1) (1999) 17–21.

[31] Y. Briend, E. Chatelet, R. Dufour, M.-A. Andrianoely, F. Legrand, S. Baudin, Dynamics of on-board rotors on finite-length journal bearings subject to multi-axial and multi-frequency excitations: numerical and experimental investigations, Mechanics & Industry 22 (35) (2021).

[32] A. R. Bartha, Dry friction backward whirl of rotors, Ph.D. thesis, ETH Zurich (2000).